Lakes_CCI+ - Phase 2 – D2.1. Product Validation and Algorithm Selection Report (PVASR)

Reference: CCI-LAKES2-0011-PVASR

Issue 2.1.1 – 17/10/2023

Contract number: 4000125030/18/I-NB –Lakes_cci

INTERNAL DOCUMENT

11 rue Hermès, Parc Technologique du Canal — 31520 Ramonville Saint-Agne, France
Tel +33 (0)5 61 39 47 00 Fax +33(0)5 61 75 10 14
www.cls.fr

CHRONOLOGY OF ISSUES

Issue	Legacy Issues	Date	Objective	Written by
1.0	1.0	19/03/2020	Initial Version	S. Simis, JF Crétaux, H Yésou, E Malnes, H Vickers, P Blanco, C Merchant, L Carrea, C Duguay, Y Wu
	1.1	24/04/2020	Revision following ESA review	See above
	2.0	30/07/2020	LSWT MODIS data processing	C Merchant
	2.1	29/09/2020	Revision following ESA review	JF Crétaux, C Merchant, H Yésou, E Malnes
2.x	2.2	02/05/2022	Updates accompanying CRDP v2.0 and v2.0.1	X Liu, JF Crétaux, L Carrea, C Duguay, S Simis
	2.3	06/07/2022	Revision following ESA review	B. Calmettes
2.1	-	06/09/2023	Revision and updates accompanying CRDP v2.1	S. Simis, B Calmettes, JF Crétaux, X Liu, A Mangili, H Yésou, L Carrea, C Duguay, Y Wu
2.1.1		17/10/2023	Revision following ESA review	S. Simis, B Calmettes, JF Crétaux, X Liu, A Mangili, H Yésou, L Carrea, C Duguay, Y Wu

Note: prior to document issue 2.1, the PVASR and ADP were provided in a combined document. From v2.1 onwards the two documents are provided separately and versioning is kept consistent with the CRDP release cycle.

Checked by	Stefan Simis – PML J-F Cretaux - LEGOS	Stefan Simis Jean-francois Cretaux
Approved by	Alice Andral - CLS	A. Andral
Authorized by	Clément Albergel - ESA	Clement Albergel

DISTRIBUTION

Company	Names	Email
ESA	Clément Albergel	clement.albergel@esa.int
BC	Carsten Brockman	carsten.brockmann@brockmann-consult.de
BC	Dagmar Müller	dagmar.mueller@brockmann-consult.de
BC	Jorrit Scholze	jorrit.scholze@brockmann-consult.de
BC	Kerstin Stelzer	kerstin.stelzer@brockmann-consult.de
BC	Martin Boettcher	martin.boettcher@brockmann-consult.de
BC	Olaf Danne	olaf.danne@brockmann-consult.de
CLS	Alice Andral	aandral@groupcls.com
CLS	Anna Mangilli	amangilli@groupcls.com
CLS	Beatriz Calmettes	bcalmettes@groupcls.com
CLS	Nicolas Taburet	ntaburet@groupcls.com
CLS	Christophe Fatras	cfatras@groupcls.com
CLS	Pierre Thibault	pthibaut@groupcls.com
CNR	Claudia Giardino	giardino.c@irea.cnr.it
CNR	Mariano Bresciani	bresciani.m@irea.cnr.it
CNR	Monica Pinardi	pinardi.m@irea.cnr.it
CNR	Marina Amadori	amadori.m@irea.cnr.it
CNR	Rossana Caroni	caroni.r@irea.cnr.it
CNR	Giulio Tellina	tellina.g@irea.cnr.it
H2O Geo	Claude Duguay	claude.duguay@h2ogeomatics.com
H2O Geo	Yuhao Wu	mark.wu@h2ogeomatics.com
H2O Geo	Jaya Sree Mugunthan	jayasree.mugunthan@h2ogeomatics.com
H2O Geo	Justin Murfitt	justin.murfitt@h2ogeomatics.com
HYGEOS	François Steinmetz	fs@hygeos.com
LEGOS	Jean-François Cretaux	jean-francois.cretaux@cnes.fr
LEGOS	Paul-Gérard Gbektom	paul.gerard.gbetkom@legos.obs-mip.fr
PML	Stefan Simis	stsi@pml.ac.uk
PML	Xiaohan Liu	liux@pml.ac.uk
PML	Nick Selmes	nse@pml.ac.uk
PML	Mark Warren	mark1@pml.ac.uk
Sertit	Hervé Yésou	Herve.yesou@unistra.fr
Sertit	Jérôme Maxant	maxant@unistra.fr
Sertit	Sabrina Amsil	s.amzil@unistra.fr
Sertit	Rémi Braun	remi.braun@unistra.fr
UoR	Chris Merchant	c.j.merchant@reading.ac.uk
Bangor	Iestyn Woolway	iestyn.woolway@bangor.ac.uk
UoR	Laura Carrea	l.carrea@reading.ac.uk
UoS	Dalin Jiang	dalin.jiang@stir.ac.uk
UoS	Evangelos Spyrakos	evangelos.spyrakos@stir.ac.uk
UoS	Ian Jones	ian.jones@stir.ac.uk

LIST OF CONTENTS

LIST OF TABLES AND FIGURES

1 Introduction

The Product Validation and Algorithm Selection Report (PVASR) reports the results of algorithm round-robin intercomparison as the basis for algorithm selection and further development during the Lakes_cci project. The PVASR is an internal document.

The purpose of the PVASR is to keep track of algorithm validation and the protocols used to carry out algorithm selection, particularly where these deviate from the Product Validation Plan (PVP).

The following elements for algorithm validation and selection are taken into consideration for each of the Lakes Essential Climate Variable products:

- How round-robin comparison was performed, including the satellite EO, ancillary and validation data sets employed.
- Specification of selection criteria to rank the results, and discussion of whether and how the selection criteria can be combined to provide an overall ranking.
- Specification of the included algorithms.
- Details of any harmonisation of the algorithms performed in advance to ensure unbiased results (e.g. common ancillary data sets).
- Results of the performance assessment of each individual algorithm.
- Ranking of the algorithms according to the results of the assessment. Different rankings may need to be derived corresponding to the different selection criteria or sets of associated selection criteria.
- Reasoning and justification of the overall ranking, including a discussion of user priorities considered when making any trade-offs in ranking.

The following sections detail these procedures for each respective Lakes ECV variable.

2 Lake Water level – LWL

2.1 Candidate algorithms

The algorithm for LWL calculation was developed at LEGOS and is detailed in the Algorithm Theoretical Basis Document (ATBD). It is based on the state-of-the-art in calculating LWL from satellite altimetry. Since each altimeter provides a distinct Global Data Record, an initial phase of organising the data and the geophysical corrections is required to produce a coherent climate data record. Moreover, each satellite mission presents a specific altimeter bias which requires correcting (based on published results), in order to arrive at a consistent long-term multi-satellite LWL time series.

The software used in this process was previously developed and is named *Hysope*. It can be used operationally and is based on Intermediate Geophysical Data Records (IGDRs) (delivery delay 1 to 2 days). It is operated at CLS in the framework of the Hydroweb database. A version for non-operational use also runs at LEGOS and is based on the same equations but using Geophysical Data Records (GDRs) instead of IGDRs (Crétaux et al. 2016).

The procedure is run against data within a priori defined polygons of lake contours (using the common dataset of maximum water extent outlines created for Lakes_cci) which are then processed using the Hysope software which is classically using the following equation:

$$LWL = Alt - Rcorr - TE \qquad [2.1]$$

Where LWL is considered with respect to a geoid, Rcorr is the measured range between the satellite and the lake surface, Alt is the altitude of the satellite above an ellipsoid and TE is the combination of all correction factors to take into account atmospheric refraction (propagation in the ionosphere and the troposphere), tidal effects (solid Earth, lake and polar), and geoid height above the ellipsoid. For more detailed information a full discussion of the computation of LWL is found in Crétaux et al. (2009).

All corrections are released in the Geophysical Data Records (GDRs) (delivery delay = 90 days) or the IGDRs. The range is chosen from different retracking considering that generally the OCOG retracking is the most suitable for continental surface (see E3UB v2.1.1 document). The geoid correction is calculated using the repeat track technique (see E3UB v2.1.1 and Crétaux et al. 2009, 2016).

2.2 Validation results

The general algorithm used to calculate water level over lakes is well known and established in scientific literature. To address the issues that are listed in the following sections, we need to analyse lakes where reference in-situ data is available. Examples of these procedures are given in Ricko et al. (2012) and Arsen et al. (2015), comparing different databases which include lake water level observations.

Lakes_cci cooperates with the State Hydrological Institute of St Petersburg, which provides in-situ data of LWL for a set of Russian and central Asian lakes. We also use existing databases on the web to increase the number of lakes that can be used for this purpose. These external sources are indicated in Table 1.

Table 1. in-situ datasets used in the validation of the LWL product

Source	Description
U.S. Army Corps of Engineer[3]	The U.S. Army Corps of Engineer provides in-situ data on Great Lakes. All levels are referenced to the International Great Lakes Datum of 1985 (IGLD 85). Water levels have been coordinated with Canada for 1918-2018.

Source	Description
Hidricos Argentina[4]	The database base of Hidricos Argentina provides in-situ data on national rivers and lakes.
U.S. Geological Survey[5]	The USGS investigates the occurrence, quantity, quality, distribution, and movement of surface and underground waters, and disseminates the data to the public. It provides in-situ data on U.S. lakes.
Water Office of Canada[6]	The Water Office of Canada provides historical water level collected over thousands of hydrometric stations across Canada.
FOEN[7]	The Swiss Federal Office for the Environment provides hydrological data, and in particular the water levels of lakes in Switzerland.
ANA[8]	The Brasilian "Agencia Nacional de Aguas e Saneamiento Basico" (ANA) provides in-situ data on reservoirs in Brazil.

The comparative analysis allows the statistically best performing retracking algorithm to be selected, as has been widely demonstrated for lakes as well as rivers.

Additional metrics to validate the LWL products include comparison of individual LWL retrieval to the long-term LWL variability, to detect outliers. The impact of removing outliers is traced as part of this process.

2.3 Identified issues

There are two main issues currently under investigation for processing of altimetry data over lakes. The first is related to the onboard tracking system, and the second is related to the processing of altimetry over small lakes.

We have identified solutions to address onboard tracking issues based on new a priori information. For retrieval of LWL over small lakes we identify solutions based in new algorithms for SAR data. Both approaches are detailed in the Algorithm Development Plan.

Another separate consideration of retrieval performance is the calculation of relative biases when several satellites of different types of orbits are used over a given lake. When we use a series of satellites such as Topex / Poseidon, Jason-1/2/3, we collect data from the same orbit, so that the relative bias between each mission is well described and calibrated (see Cretaux et al. 2009, 2011, 2013, 2018, Bonnefond et al., 2018). When observations from different orbit are used, however, such as with Jason and Envisat or Jason and Sentinel-3, another bias is added. The instrumental biases are known, but since the tracks do not cover the same position over the lake, an additional bias due to geoid error has to be considered. A very simple method has been developed at LEGOS to correct for this additional bias. The LWL is calculated independently using each track, over the whole period of time, and during the overlapping period we interpolate the point measurement from each pass and calculate the average difference between all interpolate points. It then corresponds to the additional bias due to geoid errors.

The observed limitations are not negligible and need further improvements over the next two years. The most notable expected improvement is a dedicated DEM uploaded to current ESA altimetric missions, to improve the radar tracking over small lakes particularly in regions with surrounding relief, like mountain areas. New processing of past missions, mainly using data generated as part of the FDR4ALT project contained in the TDP- IW (Thematic Data Product - Inland Waters), will also be carried out in order to provide longer and more accurate time series for small lakes. Finally, we are implementing new methods for SAR processing on sentinel-3A and sentinel-3B satellite known as full SAR processing, which will allow sub meter resolutions along the track of the satellite.

2.4 References

Arsen, A., JF. Cretaux, and R. Abarca-Del-Rio. (2015). Use of SARAL/AltiKa over mountainous lakes, intercomparison with Envisat mission J. of Adv. Space Res. The Saral/ALtiKa satellite Altimetry Mission, 38, 534-548. doi: 10. 1080/01490419. 2014. 1002590

Bonnefond, P. ; Verron, J. ; Aublanc, J. ; Babu, K. N. ; Berge-Nguyen, M. ; Cancet, M. ; Chaudhary, A. ; Cretaux, J-F. ; Frappart, F. ; Haines, BJ. , Laurain, O. ; Ollivier, A. ; Poisson, JC. ; Prandi, P. ; Sharma, R. ; Thibaut, P. ; Watson, C. (2018). The benefits of the Ka-Band as evidenced from the SARAL/AltiKa Altimetric mission: quality assessment and unique characteristics of AltiKa data, Remote Sensing 10(1), 83. doi: 1039/rs/10010083

Crétaux, J. F., S. Calmant, V. Romanovski, et al. (2009). An absolute calibration site for radar altimeters in the continental domain: lake Issykkul in Central Asia, Journal of Geodesy 83 (8) 723-735. doi: 10.1007/s00190-008-0289-7

Crétaux, J. F., S. Calmant, V. Romanovski, et al. (2011). Absolute Calibration of Jason radar altimeters from GPS kinematic campaigns over Lake Issykkul, Marine Geodesy, 34 : 3-4, 291-318. doi: 10.1080/01490419. 2011. 585110

Crétaux J-F., Bergé-Nguyen M., Calmant S., Romanovski V. V., Meyssignac B., Perosanz F., Tashbaeva S., Arsen A., Fund F., Martignago N., Bonnefond P., Laurain O., Morrow R., Maisongrande P., (2013). Calibration of envisat radar altimeter over Lake Issykkul, J. Adv. Space Res., Vol 51, 8, 1523-1541. doi: 10. 1016/j. asr. 2012. 06. 039

Cretaux J-F, M. Bergé-Nguyen, S. Calmant, N. Jamangulova, R. Satylkanov, F. Lyard, F. Perosanz, J. Verron, A. S. Montazem, G. Leguilcher, D. Leroux, J. Barrie, P. Maisongrande and P. Bonnefond. (2018). Absolute calibration / validation of the altimeters on Sentinel-3A and Jason-3 over the lake Issykkul, Remote sensing, 10, 1679. doi:10. 3390/rs10111679

Egido A., and W. H. F Smith. (2017). Fully Focused SAR altimetry: Theory and Applications, IEEE, 55, 1

Ričko M., C. M. Birkett, J. A. Carton, and J-F. Cretaux. (2012). Intercomparison and validation of continental water level products derived from satellite radar altimetry, J. of Applied Rem. Sensing, Volume 6, Art N°: 061710. doi: 10. 1117/1. JRS. 6. 061710

3 Lake water extent -LWE

3.1 Candidate algorithms

As detailed in the Algorithm Theoretical Basis Document, based on results obtained in previous work an approach based only on optical HR imagery was adopted for LWE. Water surfaces are extracted from the images based on the exploitation of an in-house processing chain, named ExtractEO (Maxant et al, 2022).

3.2 Validation results

Validation of the LWE product already starts during several preprocessing and processing steps. The validation is done individually over each lake for the following steps:

- Data selection process
- Hypsometric curves computation
- Water extraction

3.2.1 Date selection for candidate images based on altimetric data.

The aim of this step is to select set of pertinent images acquired at representative stages of a given lake, i.e., lower, higher and intermediate level of water/filling of the lake. For this, an analysis of a LWL from Hydroweb is done, based on quantile, a buffer is applied to enlarge the epochs.

In the example of Bagré reservoir (Burkina Faso), 56 dates were identified to characterize lake water level stages. Applying a temporal window to each date, the image search then extended to 336 individual days. From these dates, 110 Sentinel-2 MSI were found and investigated. After running ExctractEO to calculate cloud cover percentage, 32 images were kept with < 5 % cloud cover over the lake. The representativeness of the resulting set of images was then checked to ensure that the full range of water levels was still included (Figure 1). A hypsometric relationship is then computed based on LWL from Hydroweb and LWE derived from the Sentinel-2 MSI imagery.

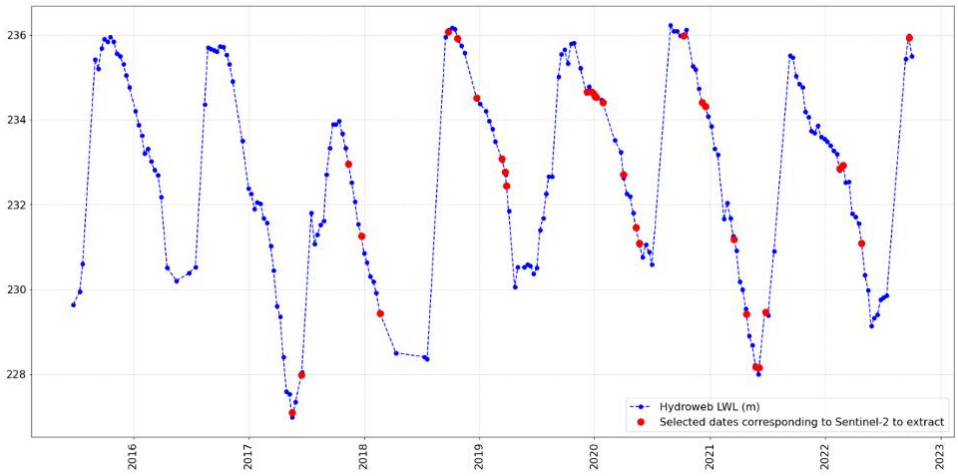

Figure 1: Date selection based on Hydroweb altimetric time series. The selected dates well cover all the stages of the lake filling, from Min to Max plus intermediate levels

3.2.2 Analysis of the hypsometric curves

The obtained hypsometric curve and repartition of the LWE/LWE pairs are analysed to observe the tendencies of the curves and identify possible anomalies, to remove outliers and to understand sources of potential omission or commission during the processing of the data (Figure 2).

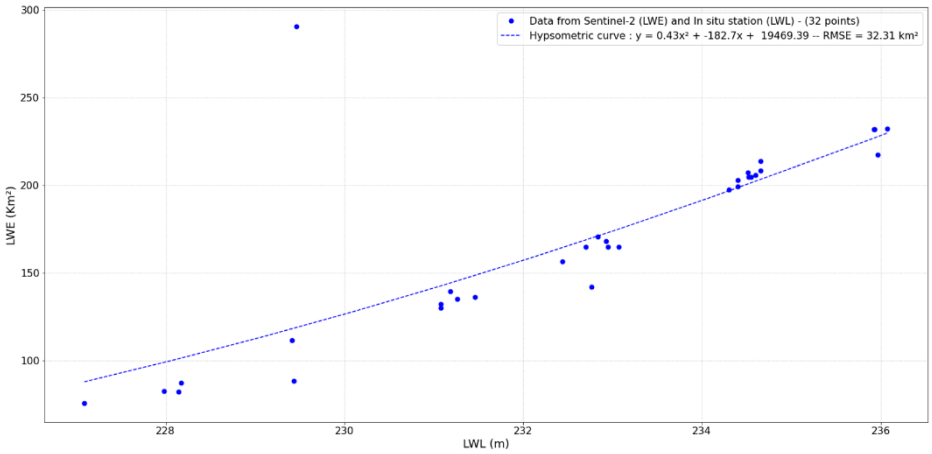

Figure 2: First estimate of the hypsometric relationship based on 32 images of Bagré Reservoir.

In this first hypsometric curve estimate, based on 32 LWL/LWE pairs, a few points are marked as outliers. It can further be noted that the curve does not integrate the highest values LWE/LWL. The resulting RMSE is relatively high at 32.31 km² (i.e., 13% of the largest observed lake surface).

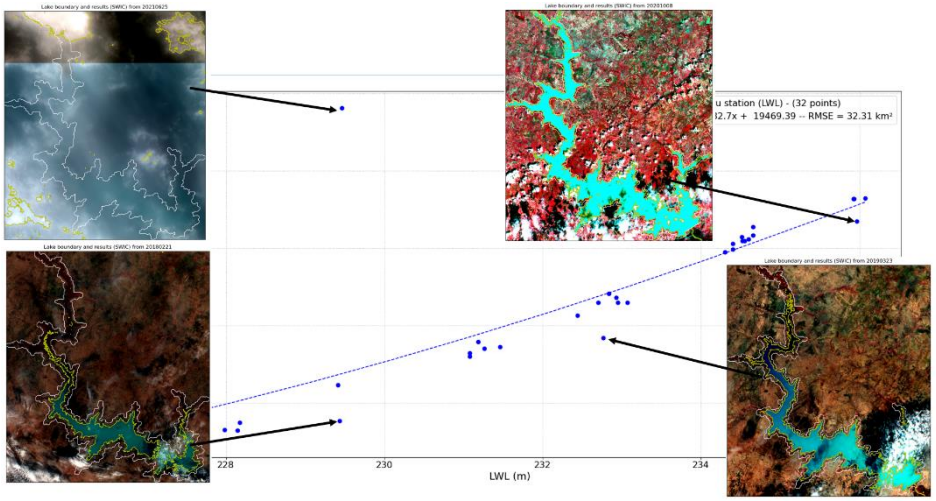

Figure 3: Analysis of problematic LWE/LWL pairs, usually related to haze, smoke or cloud.

Based on visual analysis (Figure 3), four pairs were rejected where clouds, haze and sun glint are observable.

A new hypsometric relationship is then calculated (Figure 4), where the curve extends over the full observed range and RMSE reduced from 32.3 km² (i.e. 13%) to 3.4 km² (1.4 %).

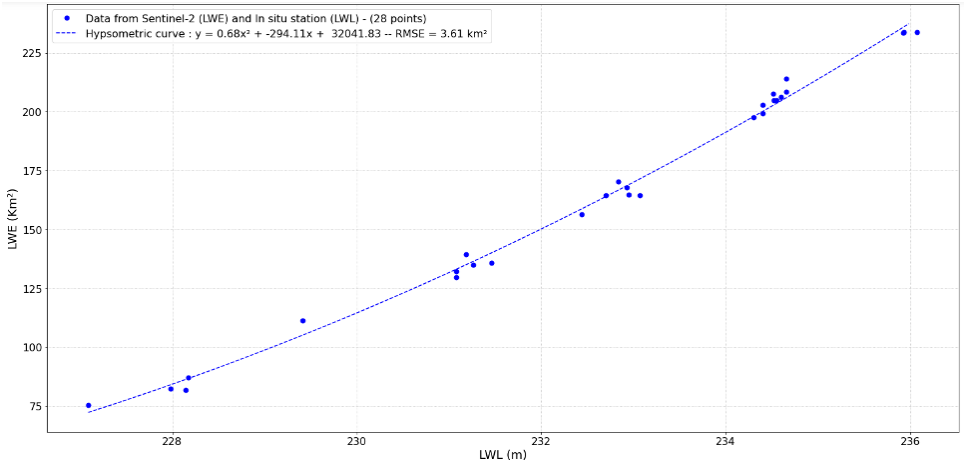

Figure 4: Final hypsometric curve for Bagré reservoir based on 28 pairs passing quality checks.

3.2.3 Water extraction process validation

Lake by lake water extents' validation is not suitable when applied to many lakes, however, it is possible, necessary and important to validate the procedure which generates lakes' area and lakes' vectors from Sentinel-2 MSI and Landsat images.

To validate the ExtractEO processing chain, cross-validation of coincident high resolution (HR) and very high resolution (VHR) optical measurements of water extent were carried out over selected lakes representing different lake environments and morphological complexity.

The result of this validation is a pixel-wise accuracy estimate, as well as overall aggregated accuracy estimates. Thus, by combining pairs of HR and VHR observations we can make an overall comparison of how good the process to generate water extent from HR optical imagery. The VHR data are either Pleiades HR or Pleiades NEO data with spatial resolution of 70 and 30 cm, respectively. This dataset (Table 2) was obtained thanks to CNES facilities within the SWOT Cal/Val program and through Pleaides NEO promotional use in the Dinamis programme. Results of the investigation are detailed for each of the regions in the following sections.

Table 2: Pairs of VHR and HR data available for the validation of the processing chain

Site	Province Country	Size in km²	VHR dataset	Dates of acquisition VHR	Dates of acquisition HR
Fitri lake	Chad	200-1250	Pleiades HR: 0,7m	2021	
Fern Ridge Reservoir	Oregon	36	Pleiades HR: 0,7m	25072022	26072022
	USA			29072022	29072022
			SPOT 6-7: 1,5 m	11082022	13082022
Lac de Der	Champagne France	10-40	Pleiades HR: 0,70m	30122019	31122019
				06012020	06012020
Lac d'Orient	Champagne France	8-23	Pleiades NEO: 0,30m	15122022	13122022
					16122022
Lac d'Auzon-Temple	Champagne France	7-20	Pleiades NEO: 0,30m	15122022	13122022
					16122022
Lac d Amance	Champagne France	0-18	Pleiades NEO: 0,30m	15122022	13122022
					16122022

Shenjing lake	Anhui Prov. PR China	33	Pleiades NEO: 0,30m	10122021	07122021

Lakes in Champagne

In this area, several lakes are linked to the flood protection system of Paris by the Grands lacs de Seine establishment (Figure 5). They were covered by the recently launched Pleiades NEO sensors as well by Pleaides imagery.

Figure 5: Lakes in Champagne

Pleiades NEO was acquired on 15 December 2022 whereas Sentinel-2 MSI data were acquired on 13 and 16 December 2022. Due to presence of snow, the comparison was carried out for the VHR/HR pair of 15 and 13 December 2022. This winter period corresponds to low water level, when open water is surrounded by sandy-muddy banks. This offers a good opportunity to illustrate the classical effects related to the different spatial resolution, with a sawtooth/staircase limit on Sentinel2 LWE compared to the straighter limits of VHR shown in Temple Lake (Figure 6). This comparison also highlights the apparent commission related to the exploitation of the SWIR band from Sentinel-2, shown in detail for Orient Lake (Figure 7). At this low water level, SWIR bands are not so effective at differentiating water from the surrounding environment, and do not separate wet sandy-muddy banks from open water.

Figure 6: Effect of resolution in Temple Lake. The red line marks LWE from Pleiades NEO (30cm); the yellow line shows the saw tooth limits derived from Sentinel-2 MSI.

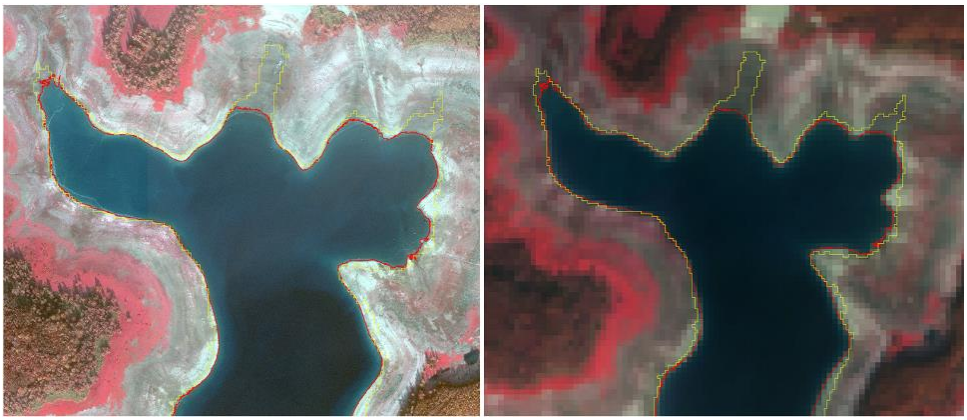

Figure 7: Comparison of VHR/HR in Orient Lake. Left: Pleaides NEO. Right: Sentinel-2. Red lines are the LWE limits derived from Pleaides NEO, yellow lines the Sentinel LWE limits.

Table 3: Metrics obtained over the Champagne lakes

All			
Metric	FREQUENCY	Area m²	Percentage
reference	72	21693449,96	100,00
database	23	21800055,36	100,49
omission	72	570486,23	2,63
commission	23	677091,66	3,11
taux_detection	17	21122963,70	97,37
taux_justesse	1	999999,00	96,89
BREAK	1	1,00	1,00
precision	1	1,00	0,97
recall	1	1,00	0,97
Fscore	1	1,00	0,97
CSI	1	1,00	0,94

Amance			
Metric	FREQUENCY	Area m²	Percentage
reference	20	1819683,51	100,00
database	6	1903600,00	104,61
omission	20	56409,20	3,10
commission	6	140325,68	7,37
taux_detectio	3	1763274,32	96,90
taux_justesse	1	999999,00	92,63
BREAK	1	1,00	1,00
precision	1	1,00	0,93
recall	1	1,00	0,97
Fscore	1	1,00	0,95
CSI	1	1,00	0,90

Auzon Temple			
Metric	FREQUENCY	Area m²	Percentage
reference	25	8711286,40	100,00
database	8	8473200,00	97,27
omission	25	338141,24	3,88
commission	8	100054,90	1,18
taux_detectio	6	8373145,10	96,12
taux_justesse	1	999999,00	98,82
BREAK	1	1,00	1,00
precision	1	1,00	0,99
recall	1	1,00	0,96
Fscore	1	1,00	0,97
CSI	1	1,00	0,95

Orient			
Metric	FREQUENCY	Area m²	Percentage
reference	13	10829060,28	100,00
database	3	11147755,36	102,94
omission	13	96436,30	0,89
commission	3	415131,38	3,72
taux_detectio	2	10732623,98	99,11
taux_justesse	1	999999,00	96,28
BREAK	1	1,00	1,00
precision	1	1,00	0,96
recall	1	1,00	0,99
Fscore	1	1,00	0,98
CSI	1	1,00	0,95

The metrics obtained on these reservoirs show very high values both for the classic precision and accuracy rates and for the more interesting parameters such as the F_Score and Recall. This reflects the very good recognition and extraction of water bodies using Sentinel2 data via ExtractEO, qualifying the proposed approach for generating LWEs (Table3).

Fern Ridge reservoir (Oregon, USA)

Fern Ridge Reservoir (or Fern Ridge Lake) is a reservoir on the Long Tom River in Oregon (USA). The reservoir is a U.S. Army Corps of Engineers flood control project encompassing near 49 km² and a popular site for boating, fishing, and birdwatching. Surrounding portions of the reservoir is the Fern Ridge Wildlife Area, a wildlife management area providing a unique habitat for a variety of species including wintering waterfowl populations.

By comparing the LWE extracted from the VHR and HR images, Sentinel-2 detected more water in the eastern part of the reservoir (Figure 8)..These pixels, corresponding to wet areas of mixed waterlogged vegetation located in the Ridge Fire zone, were extracted and recognised as water areas from the Senitnel2 data. This confusion between open water and wetland stems from the use of the Sentinel2 SWIR bands, spectral bands which are highly discriminating for open water, but which make it difficult to differentiate these wetlands from waterlogged areas, just as in other cases from sand or mud banks. In the case of the Fern Ridge site, this relative commission represents around 4% of the water surface.

This case also illustrates the problem of the definition of a lake, what are the limits of a water body of the zones of open water only or zones of open water plus the surrounding flooded wetlands ?.

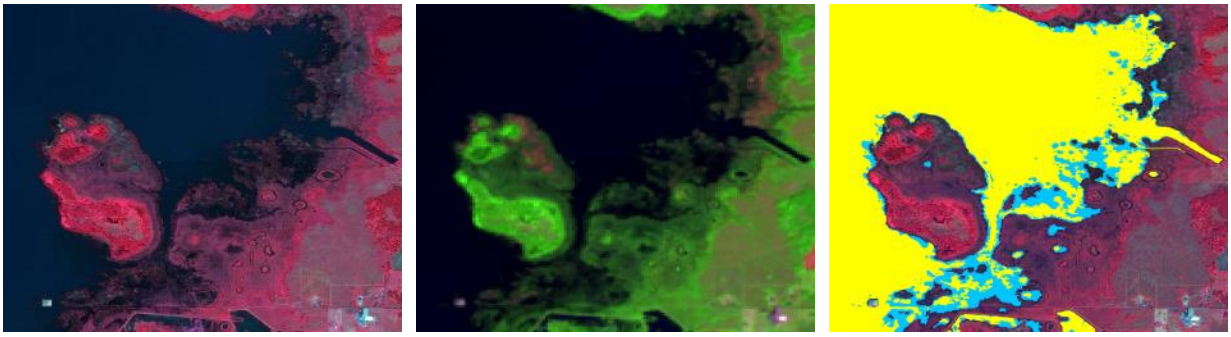

Figure 8: Fern Ridge reservoir observed with Pleiades HR (25-07-2022), Sentinel-2 SWIR false colour composite (26-07-2022). A comparison of LWE derived from Pleiades in yellow and Sentinel-2 in blue is shown to the right.

In terms of metrics, despite this relative omission related to wetlands, correspondence was good in terms of accuracy and F Score (Table 4).

Table 4: Metrics obtained over Fern Ridge reservoir for the VHR/HR pairs of the Pleiades and Sentinel-2 on 26/07/2022 and 25/07/2022 (left), and for Pleiades and Sentinel-2 acquired on 29/07/2022 (right).

	Pleaides on 526/07/2022, S-2 on 25/07/2022				Pleaides and S-2 on 629/07/2022		
Type	Frequency	Sum Area	Percent		Frequency	Sum Area	Percent
Reference	91	27242769.9	100		102	27205236.4	100
Database	42	28411100.	104.29		51	28188500.	103.61
Omission	84	347057.1	1.27		94	350991.15	1.29
Commission	42	1515387.2	5.53		50	1334254.74	4.73
Detection rate	31	26895712.8	98.73		36	26854245.2	98.71
Accuracy rate	1	999999.0	94.67		1	999999.0 1.0	95.27
Break	1	1.0	1		1	1.0	1
Precision	1	1.0	0.95		1	1.0	0.95
Recall	1	1.0	0.99		1	1.0	0.99
F_score	1	1.0	0.97		1	1.0	0.97
CSI	1	1.0	0.94		1	1.0	0.94

Fitri Lake (Chad)

Fitri Lake (12°50'N, 17°30'E), is the largest lake inside Chad. It plays a major role in this Sahel region for human activities and as a refuge for biodiversity. It occupies an endoreic watershed with a surface area of 80,000 km^2 located in the middle of the Sahel to the east of Lake Chad. Fitri Lake's dynamic is directly linked to the West African monsoon regime, whose seasonal to multi-annual variability directly impacts variations in its level and its extent. As a result, Lake Fitri is a sensitive and unique record of monsoon variability and its impact on landscapes and ecosystems in the past.

Lake Fitri is an endoreic lake occupying a basin with a very shallow topography. The depth of the lake is less than 2.5 m (low-water period). From 1995 onwards, based on Landsat data, a gradual resurgence of the lake and its wetland was observed. Observations in recent years (2017-2022) confirm the trend towards increased extension of the lake during the rainy season. These analyses were carried out using Sentinel-2 satellite images with a resolution of 10 m (Maxant et al., 2023). They clearly highlight the

surplus hydrological years of 2020 and 2022, with water surfaces of 1249 and 1180 km² respectively, compared with the 194 km² observed in 2017.

Over Fitri Lake (Chad), two approaches of processing Sentinel-2 MSI were compared, one based on 10 m spatial resolution and the other at 20 m of spatial resolution.

Visual analysis highlighted the gain related to the highest spatial resolution of Pleaides. This is particularly well documented on the fringes of the main water body but also on smaller flooded branches of the lake (Figure 9 and Figure 10).

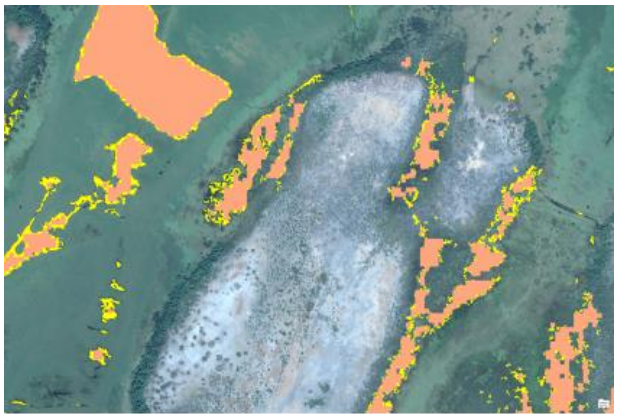

Figure 9: Fitri lake illustration of gain in water surface when exploiting VHR Pleiades imagery (yellow) compared with the Water mask derived from Sentinel-2 (orange).

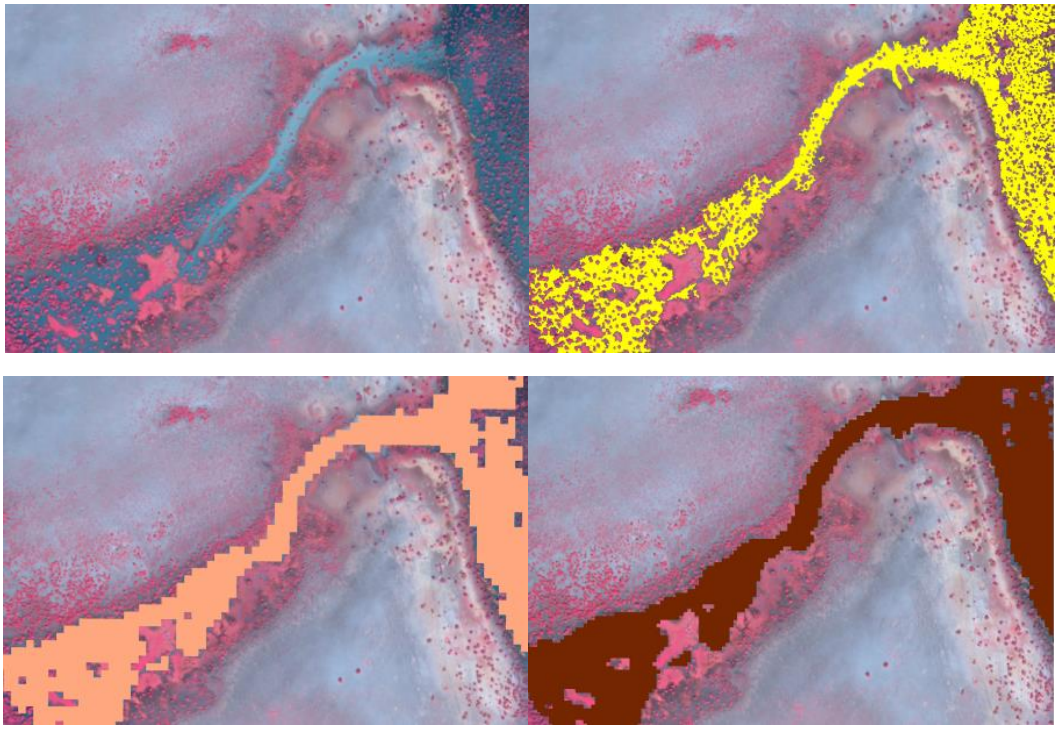

Figure 10:Comparison of LWE derived from Pleaides image and Sentinel 2 with UL, Pleiades colour composite of a flood branch of the Fitri lake, upper right, LWE derived from Pleaides, Bottom left, LWE derived from a Sentinel2 image at 20 m of spatial resolution and bottom right, LWE from A Sentinel2 processed at 10m.

When analysing the obtained LWE metrics (Table 7), values are very similar between the two image resolutions, with slightly higher omission at 20 m and slightly more commission at 10 m. At both Sentinel-2 resampled resolutions, the recall and precision are relatively good for this complex hydro- system. Of course, part of the omission is related to the difference in spatial resolution between the VHR and HR images.

Table 7: Metrics obtained from the comparison of LWE derived from Pleiades and Sentinel 2 MSI at 20 m (left), and 10 m (right).

	S-2 20m versus Pleiades				S-2 10m versus Pleiades		
Type	Frequency	Sum Area	Percent		Frequency	Sum Area	Percent
Reference	63797	370516696.8	100		63797	370516696.8	100
Database	7629	353542800	94.42		8193	361739810.3	97.6
Omission	62591	48843863.9	13.18		94	46444991.5	12.53
Commission	7459	31869966.8	9.01		50	37668104.8	10.41
Detection rate	7353	321672833.1	86.82		36	32417105.3	87.46
Accuracy rate	1	999999.0	90.99		1	999999.0	89.59
Break	1	1.0	1		1	1.0	1
Precision	1	1.0	0.91		1	1.0	0.90
Recall	1	1.0	0.87		1	1.0	0.87
F_score	1	1.0	0.89		1	1.0	0.86
CSI	1	1.0	0.80		1	1.0	0.79

Shenjin Lake

Shengjin Lake, located on the south bank of the middle and lower reaches of the Yangtse River (Anhui province, PR China) is a large shallow freshwater lake with a shoreline extending to 156 km at 11 m above sea level. Dominated by lakes and freshwater marshes and boasting good water quality, it is one of the best-preserved inland freshwater lake systems along these stretches of the Yangtze River. The site plays a role in regulating floods along the Yangtze and contributes to water purification and regional climate regulation. It also provides an important stopover and wintering ground for migrating birds.

The case of the Shenjin Lake illustrates the difficulties to extract water extent in case of shallow waters, when the delimitation of water and wet sediments can be very delicate. This is particularly sensitive during the step of sampling selection process.

For Sentinel-2, two sets of parameters were tested (Table 8), to reduce the weight of the SWIR channels that can induce commission over wetland and mud/sandy banks such as previously shown.

Table 8: Parameters exploited for sampling selection

	Param 1	Param 2
MNDWI Threshold	0.45	0.1
NDWI Threshold	[0.1, 0.4]	[0.01,0.3]
Number of samples	10000	10000
Pekel Threshold	20	20
Refining method	SWIC	SWIC
SWIC Threshold	[0.3, 0.9]	0

When analysing the LWE limits derived from Pleaides NEO and the two LWE results from Sentinel-2, the limits of the Pleaides NEO and Sentinel-2 with parametrization 1 are generally very similar, whereas the LWE obtained with the second set parameterization introduce a buffer zone along the water limits, including very light sandy areas (Figure 11).

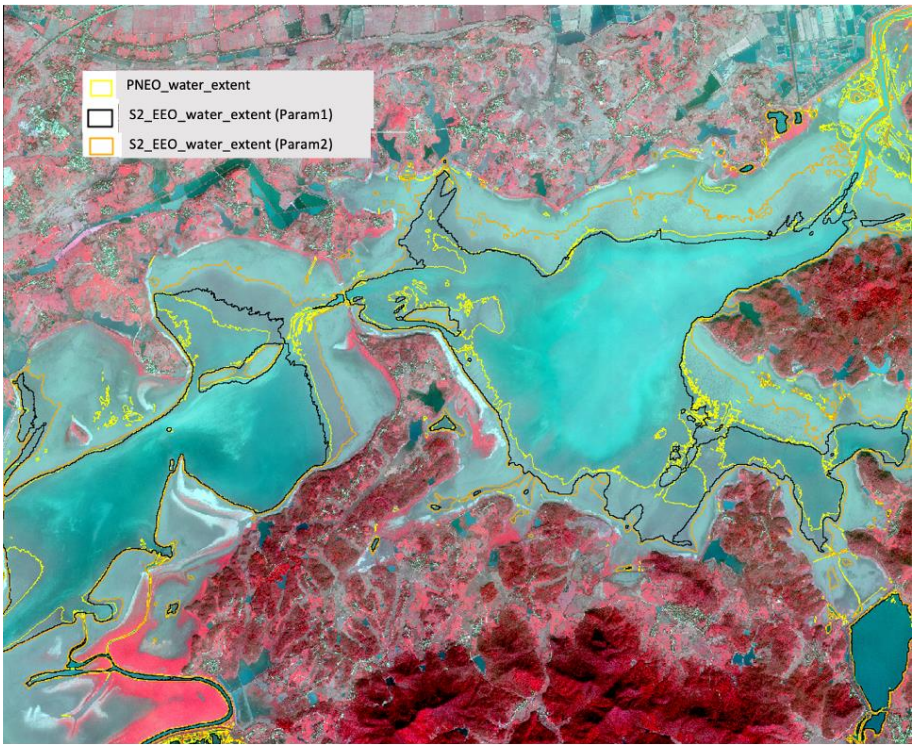

Figure 11. Comparison of the LWE limits derived from Pleiades NEO and Sentinel2

When analysing the LWE metrics (Table 9), results obtained from parameter set 2 present high values for commission and relative low accuracy values. The commission rate decreases with the first parametrization while omission increases. These omissions are mostly related to very fine water paths observed at 0.30 cm and not at 10 m resolution. Over this complex shallow water system, the different scores are relatively good with recall or F Score values about 0.85-0.87.

Table 9: Metrics obtained from the comparison of the LWE derived from Pleaides Neo and two parametrizations of the sampling step for water recognition from Sentinel-2.

	Parametrization 1			Parametrization 2		
Type	Frequency	Sum Area	Percent	Frequency	Sum Area	Percent
Reference	513	32691145.8	100	513	32691145.8	100
Database	41	33698468.7	103.8	102	46942058	143.59
Omission	442	4099507.1	12.54	333	1155269.43	5.53
Commission	30	5106830	15.15	100	15406181.6	32.82
Detection rate	36	28591638.7	87.46	69	31535876.3	96.47
Accuracy rate	1	999999.0	84.85	1	999999.0	67.18
Break	1	1.0	1	1	1.0	1
Precision	1	1.0	0.85	1	1.0	0.67
Recall	1	1.0	0.87	1	1.0	0.96
F_score	1	1.0	0.86	1	1.0	0.79
CSI	1	1.0	0.75	1	1.0	0.66

3.3 Identified issues

In terms of algorithm few issues have been identified:

- The presence of sun glint on water surfaces can disrupt the process of recognising and extracting water bodies. The appearance of this phenomenon depends not only on the position of the sun, but also on the location of the target in the swath. It would be beneficial to develop a sunglint flag to avoid issues with sunglint propagating through to final results. This would also allow automatic adjustment of related coefficients and thresholds in the ExtractEO processing chain.
- Refinement to the existing cloud detector in the ExtractEO chain should lead to better cloud detection in the S-2 L2A product.

3.4 References

Maxant J, Braun R, Caspard M, Clandillon S. (2022). ExtractEO, a Pipeline for Disaster Extent Mapping in the Context of Emergency Management. Remote Sensing. .14(20):5253. https://doi.org/10.3390/rs14205253

4 Lake surface water temperature – LSWT

4.1 Candidate algorithms

Surface temperatures from infrared observations are obtained by coefficient-based methods or optimal estimation (OE, Merchant and Embury 2014). Because of the varied altitudes of lakes and the large differences in atmospheric absorption associated with continentality, optimal estimation is the appropriate approach for LSWT estimation (MacCallum and Merchant, 2012).

OE also provides comprehensive equations for uncertainty evaluation, on which basis uncertainty estimates are provided in LSWT products per datum.

As well as retrieval, classification of which pixels are filled with water under clear skies is a necessary part of the LSWT processing. This is done by a "fuzzy logic" style approach in which a number of metrics with fuzzy thresholds are combined into a "water detection score" that contributes to the definition of the quality level attributed to the pixel. Bayesian cloud detection, as used for sea surface temperature, was also considered to identify clear-sky pixels but is heavily compromised in its current implementation for small lakes, where the spatial coherence of the temperature of the scene is not a good indicator of cloud (unlike in the centre of large lakes and over open ocean). Because of the user requirement to increase the number of measured lakes, the latter scheme is therefore currently inapplicable for the identification of clear-sky only water pixels.

4.2 Validation results

Validation results (for LSWT 4.5 for the CCI Lake v2) are summarised in the product validation report. The validation undertaken is a comparison of satellite to matched in-situ temperatures. These comparisons are limited by the non-representative sample-of-opportunity (in-situ measurements being unfortunately hard to obtain) and by variable and often unknown in-situ uncertainty characteristics and quality control. Validation results are too ambivalent in this case to be used as a discriminant between alternative algorithmic approaches, and for LSWT are not used in this way. As mentioned in the previous section, the retrieval algorithm is established by considerations rooted in physics and inverse theory.

Nonetheless, the validation exercise is sufficient to establish that for quality level (QL) 5 (best quality) LSWT data, the data have low bias (<0.1K) and uncertainty estimates are reasonable.

4.3 Identified issues

LSWT retrieval

1. Optimal estimation uses an observation-simulation error covariance matrix. This matrix is presently a simple diagonal estimate that doesn't account for the likelihood of cross-channel correlations in the simulation errors.
2. Optimal estimation uses a prior error covariance matrix. This matrix is a simple diagonal estimate based on experience of ERA-interim, and ideally should be updated for use with ERA-5.

LSWT retrieval uncertainty

(NB, this aspect is also addressed by the issues identified for LSWT retrieval.)

1. The decomposition of the optimal estimation uncertainty into different correlation length scales is an approximation; a more complete solution needs to be coded. (The decomposition is relevant when creating gridded data.)

Water detection

1. The water detection to select water-only pixels relies on day-time (reflectance) channels, and therefore cannot be applied at night. The alternative that may work at night is based on Bayesian cloud screening (as used in SST CCI), and for small lakes require considerable research, development and modification which will be explored for the CCI LAKES v3 dataset.

Quality level determination

1. QL determination is based mainly on water detection results, on the sensitivity to the prior, on retrieval chi-square results (which measure the plausibility of the solution given the prior and observations). However, the chi-square results differed more than expected between Metop-A and Metop-B AVHRRs, affecting the QL attribution adversely in the case of Metop-B. This is yet to be clearly understood, but the root of the reasons very likely lies in the L1b data.

Increasing coverage processing night-time

1. By far the most impactful issue for users for LSWT is to increase the density of coverage, which is limited by sensor-orbit coverage and by cloud cover. Moreover, night-time observations are considered to provide better accuracy than daytime data when compared with bulk temperatures due to, among other things, the absence of solar heating (Hook et al., 2003). Therefore, in v5.0 an attempt to generate night-time LSWT will be undertaken by the team.
2. Without guaranteeing success, Bayesian cloud detection (adapted from SST CCI) will be applied on night-time observations, based on developing a new climatology of LSWT from the CDR v2.1. If validation of the night-time results justifies their inclusion in v3.0, this will approximately double the observation frequency for some lakes (not necessarily all).

A work-around for the Metop-B issue with chi-square is implemented in LSWT v4.1 and LSWT v4.5, but a more fundamental resolution will be sought.

4.4 References

Merchant, C.J., Embury, O., Roberts-Jones, J., Fiedler, E., Bulgin, C. E., Corlett, G. K., Good, S., McLaren, A., Rayner, N., Morak-Bozzo, S. and Donlon, C. (2014) Sea surface temperature datasets for climate applications from Phase 1 of the European Space Agency Climate Change Initiative (SST CCI). Geoscience Data Journal, 1 (2). pp. 179-191.

MacCallum, S.N. and Merchant, C.J. (2012) Surface water temperature observations of large lakes by optimal estimation. Canadian Journal of Remote Sensing, 38 (1). pp. 25-45.

Hook, S. J., Prata, F. J., Alley, R. E., Abtahi, A., Richards, R. C., Schladow, S. G., Palmarsson, S. (2003). Retrieval of lake bulk and skin temperatures using Along-Track Scanning Radiometer (ATSR-2) data: A case study using Lake Tahoe, California. Journal of Atmospheric and Oceanic Technology, 20(4), 534–548.

5 Lake water leaving reflectance – LWLR

5.1 Candidate algorithms

The algorithm validation procedures and results associated with CRDP v2.1 are unchanged with respect to CRDP v2.0.2. New algorithm validation work is planned for CRDP v3.0, as described in the Algorithm Development Plan. New chlorophyll-a candidate algorithms for OLCI are already described here.

Algorithms in the LWLR processing chain *Calimnos* fall into three categories:

- Pre-processing including pixel identification as water, land, cloud or ice
- Atmospheric correction yielding LWLR
- Derived water-column concentration estimates, notably of chlorophyll-a and turbidity

For the **pre-processing** category the processor relies on the Idepix multi-sensor processor in SNAP. The algorithm combines information from static sources (such as water extent) and dynamic pixel identification based on a neural network trained for each of the optical sensors. Depending on the capabilities of the sensor, the processing chain will rely on combinations of these processes. The algorithm is not part of validation of the Lakes_cci LWLR but its performance is taken into consideration with regard to consistency in water/land masking between the Lakes_cci thematic ECVs.

Validation of algorithms for **atmospheric correction** requires near-coincident in-situ observations of water-leaving reflectance. Due to scarce in-situ data from lakes, the window for 'coincidence' may be up to several days from satellite observation. Longer time windows allow more data points to be included, which is suitable to determine the best-performing algorithm but less suitable to determine product uncertainties which may then be exaggerated. The majority of radiometric in-situ data for lakes is deposited in LIMNADES, the largest and only community-owned repository for lake bio-optical measurements, correspond to the MERIS observation period. Recently, the GLORIA database (Lehmann et al. 2023) was published which provides an additional radiometric reference source, albeit with a large degree of overlap with LIMNADES. GLORIA is gradually being introduced in algorithm validation. Finally, several automated radiometry systems are currently in operation through a range of research projects, although not within a formal network. These include the WISPstation observations using instrumentation by Water Insight, and So-Rad shipborne observations with automation developed at PML. The procedure for selecting and evaluation of candidate algorithms is presently as follows:

- Round-robin evaluation of MERIS atmospheric correction algorithms
- Application of the most suitable MERIS algorithm(s) to MERIS and OLCI
- Evaluation of algorithms for MODIS based on minimizing inter-sensor bias during overlap with MERIS and OLCI, respectively

A strategy for including SeaWiFS observations will be defined based on the results of MODIS (and VIIRS), although this is not within the scope of currently planned outputs.

Finally, **algorithms for the derived water-column properties**, notably chlorophyll-a and turbidity (either directly or by conversion of total suspended matter concentration, usually following Nechad et al. 2016), are evaluated in a sensor-dependent manner similar to the procedure given for atmospheric correction algorithms. These algorithms are first evaluated against the available in-situ data archives to assess their application range. The algorithms are then tuned for optimal performance as a function of their membership to a set of **optical water types,** allowing them to be mapped to satellite imagery using a weighted averaging 'blending' method. Details on the optical water type methodology are provided in the Algorithm Theoretical Basis Document.

Several of the algorithms that may be considered for atmospheric correction are coupled atmosphere-water models yielding water-column properties including chlorophyll-a and suspended matter concentrations. These algorithms have not all been thoroughly evaluated in peer-reviewed literature and are included primarily for reference. Where they outperform better-understood alternatives they will be given further consideration.

The candidate algorithms are listed per sensor In the following tables. As a rule of thumb, only algorithms with a transparent and published methodology are considered, and algorithms with a theoretical basis suggesting specificity and sensitivity to the target substance are preferred. Where algorithms have been previously validated in a specific region, their validated range is given. The MERIS/OLCI algorithms tested for CRDP v1.0 (Table 10 and Table 11) are described in comparative detail in Neil et al. (2019).

For the MODIS/VIIRS set of candidate algorithms (Table 12 for chlorophyll-a, Table 13 and Table 14 for suspended matter and turbidity) this comparison was carried out for the first time in the Lakes_cci and used from CRDP v2.0. Details on the waveband combinations that are shown in these tables suggest there may be substantial overlap, in which case highly similar algorithms are ultimately collapsed into algorithm types prior to calibration.

Finally, Table 15 and Table 16 list candidate chlorophyll-a and TSM/Turbidity algorithms for OLCI (and in many cases, MERIS) which will be evaluated for CRDP v3.0. This analysis is not yet reported here.

Table 10: Candidate algorithms tested for MERIS (and OLCI by proxy) yielding chlorophyll-a concentration

Type	Model	Reference
(Semi-)empirical NIR-red BR	MERIS 2-Band 708/665	Gilerson *et al.* 2010 Gurlin *et al.* 2011 Gons *et al.* 2005
	MERIS 2-Band 753/665	Gilerson *et al.* 2010 Gitelson *et al.* 2011 Moses *et al.* 2009.
	MERIS 3-Band	Gitelson *et al.* 2008 Gitelson *et al.* 2011 Gurlin *et al.* 2011 Moses *et al.* 2009
	MERIS NDCI	Mishra *et al.* 2012
Empirical OC	MERIS OC2E MERIS OC3E MERIS OC4E	O'Reilly *et al.* 2000
Neural Network	NN_Chl NN_IOP FUB CoastColour C2RLakes(EUT/BOR)	Ioannou *et al.* 2013
Analytical	MERIS QAA [Turbid]	Mishra *et al.* 2013
	MERIS GSM	Maritorena *et al.* 2002
	MERIS Matrix Inversion	Boss and Roesler 2006

Type	Model	Reference
Peak Height Method	MPH	Matthews *et al.* 2012

Table 11: Candidate algorithms tested for MERIS (and OLCI by proxy) yielding total suspended matter.

Type	Algorithm name	Reference
Empirical	Binding red Zhang 708 Vantrepotte 665 POWERS 560	Binding *et al.* 2005 Zhang *et al.* 2010 Vantrepotte *et al.* 2011 Eleveld *et al.* 2008
	D'Sa 665/560 Dekker 490, 560 Dekker 560, 665	D'Sa *et al.* 2007 Dekker *et al.* 2002
	Loisel 3-Band	Loisel *et al.* 2014
(Semi-) Analytical	Binding A Nechad 665 Nechad 681 Nechad 708 Nechad 753	Binding *et al.* 2010 Nechad *et al.* 2010

Table 12: Summary of candidate Chla algorithms tested for MODIS/VIIRS

Code	Name/form	Type	Bands*	Calibration or validated range	Reference
A	OC3M	blue-green band ratio	min[R_{rs}(443), R_{rs}(488)], R_{rs}(547)	0. 2 ~ 90 mg m^{-3}	O'Reilly and Maritorena 2000
B	OC2M	blue-green band ratio	R_{rs}(488), R_{rs}(547)	0. 2 ~ 90 mg m^{-3}	O'Reilly and Maritorena 2000
C	OC2M-HI (500 m)	blue-green band ratio	R_{rs}(469), R_{rs}(555)	0. 2 ~ 90 mg m^{-3}	O'Reilly and Maritorena 2000
D	FLH	peak height	R_{rs}(665), R_{rs}(677), R_{rs}(746)	1 ~ 10 mg m^{-3}	Letelier 1996
E	linear	NIR-red band ratio	R_{rs}(748), [R_{rs}(667) or R_{rs}(678)]	4 ~ 240 mg m^{-3}	Gitelson 1992; Dall'Olmo et al. 2005; Gitelson et al. 2007, 2008; Gurlin et al. 2011
F	linear	blue-green band ratio	R_{rs}(551), R_{rs}(443)	8 ~ 17 mg m^{-3}	Ha et al. 2013
G	linear	spectral index	R_{rc}(645), R_{rc}(859)	6. 6 ~ 113. 7 mg m^{-3}	Shi et al. 2017
H	APPEL model	empirical	R(645), R(859), R(469)	2. 5 ~ 91. 0 mg m^{-3}	El-Alem et al. 2012
I	GSM	semi-analytical	(not reproduced)	0 ~ 100 mg m^{-3}	Maritorena et al. 2002

Code	Name/form	Type	Bands*	Calibration or validated range	Reference
J	QAA_v6	semi-analytical	(not reproduced)	0. 02 ~70. 21 mg m^{-3}	Lee et al. 2002
K	QAA_Tur	semi-analytical	(not reproduced)	59 ~1376 mg m^{-3}	Mishra et al. 2013, 2014
L	MODIS SA	semi-analytical	(not reproduced)	0 ~ 2 mg m^{-3}	Carder et al. 2004

*Reflectance bands are as used in the original definition, taking the following forms:
R_{rs} is above-surface remote-sensing reflectance
R_{rc} is the atmospherically Rayleigh-corrected reflectance.

Table 13: Summary of candidate Turbidity algorithms tested for MODIS/VIIRS

Code	Name/form	Type	Bands*	Calibration or validated range	Reference
A	polynomial	single red band	$R_{rs}(645)$	TSM <30 mg L^{-1}	Petus et al. 2010
B	linear	single red band	$R_{rs}(645)$	Turb 0 ~ 15 NTU	Moreno-Madrinan et al. 2010
C	exponential	single red band	$R_{rs}(645)$	Turb 1. 8 ~ 160 FTU	Constantin et al. 2017
D	power law	single red band	$R_{rs}(645)$	Turb 0. 9 ~ 8 NTU	Chen et al. 2007
E	polynomial	single NIR band	$nL_w(869)$	Turb 1~300 NTU	Wang et al. 2012
F	power law	NIR-red ratio	$R_{rs}(859)/R_{rs}(645)$	Turb 50 ~ 1000 NTU	Robert et al. 2016
G	exponential	NIR-red ratio	$R(859)/R(645)$	Turb 77. 4 ~2193 NTU TSM 77 ~ 2182 mg L^{-1}	Doxaran et al. 2009
H	semi-empirical	red or NIR	$\rho_w(645)$, $\rho_w(859)$	Turb 1. 8 ~ 988 FNU	Dogliotti et al. 2015

*Reflectance bands are as used in the original definition, taking the following forms:
R_{rs} is above-surface remote-sensing reflectance
nL_w is the normalized water-leaving radiance.
R is the 'surface reflectance' of the MODIS land product.
ρ_w is the water reflectance, which is defined as $\pi L_w(\lambda) / E^0{}_d{}^+(\lambda)$, where L_w is the water-leaving radiance and $E^0{}_d{}^+$ is the above-water downwelling irradiance.

Table 14 Summary of candidate TSM algorithms tested for MODIS/VIIRS

Code	Name/form	Type	Bands*	Calibration or validated range	Reference
I	linear	single red band	$R(645)$	0 ~ 55 mg L^{-1}	Miller and McKee 2004; Sipelgas et al. 2006
J	polynomial	single red band	$R_{rs}(645)$	0 ~ 30 mg L^{-1}	Petus et al. 2010
K	exponential	single red band	$R_{rs}(645)$	0 ~ 300 mg L^{-1}	Zhao et al. 2011; Shi et al. 2015
L	polynomial	single red band	$nL_w(645)$	0 ~ 16 mg L^{-1}	Ondrusek et al. 2012
M	exponential	NIR-red ratio	$R(859)/R(645)$	77 ~ 2182 mg L^{-1}	Doxaran et al. 2009

N	power law	NIR-red ratio	$R_{rs}(859)/R_{rs}(645)$	18 ~ 927 mg L^{-1}	Robert et al. 2016
O	polynomial	NIR-red ratio	$log[R_{rs}(859)]/log[R_{rs}(645)]$	5. 8 ~ 577. 2 mg L^{-1}	Chen et al. 2015
P	linear	NIR-red ratio	$log[R_{rs}(859)]/log[R_{rs}(645)]$	1 ~ 64 mg L^{-1}	Wang et al. 2010a
Q	exponential	red and NIR	$R_t(645)$-$R_t(859)$	0 ~ 12 mg L^{-1}	Hu et al. 2004
R	linear	red and NIR	$R_{rs}(645)$-$R_{rs}(859)$	0. 3 ~ 20 mg L^{-1}	Tarrant et al. 2010
S	linear	two NIR bands	$\rho_w(859)$-$\rho_w(1240)$	74 ~ 881 mg L^{-1}	Wang et al. 2010b
T	exponential	three bands	$R_{rs}(488)$, $R_{rs}(555)$, $R_{rs}(645)$	1~ 300 mg L^{-1}	Zhang et al. 2010
U	semi-analytical	red	nL_w (748)	0. 18 ~ 28. 3 mg L^{-1}	Binding et al. 2010
V	generic single-band	red or NIR	$\rho_w(645)$ or $\rho_w(859)$	1 ~100 mg L^{-1}	Nechad et al. 2010; Polito et al. 2016

*Reflectance bands are as used in the original definition, taking the following forms:
R is the 'surface reflectance' of the MODIS land product.
R_{rs} is above-surface remote-sensing reflectance
R_t is the total radiance observed by MODIS (F_t) divided by the annual mean extraterrestrial solar irradiance F_0.
nL_w is the normalized water-leaving radiance.
ρ_w is the water reflectance, which is defined as $\pi L_w(\lambda) / E^0{}_d{}^+(\lambda)$, where L_w is the water-leaving radiance and $E^0{}_d{}^+$ is the above-water downwelling irradiance.

Table 15 Summary of candidate new Chla algorithms for OLCI

Algorithm	Architectural approach	Formular	Original training (mg.m-3)	reference
OC4_OLCI	Blue-green ratios	MBR=Rrs(443>490>510)/Rrs560	0.01 to 78	(O'Reilly and Werdell 2019)
OC5_OLCI	Blue-green ratios	MBR=Rrs(413>443>490>510)/Rrs560	0.01 to 78	(O'Reilly and Werdell 2019)
OC6_OLCI	Blue-green ratios	MBR=Rrs(413>443>490>510)/M(560&665)	0.01 to 78	(O'Reilly and Werdell 2019)
OC4_MERIS	Blue-green ratios	MBR=Rrs(442>490>510)/Rrs560	0.01 to 78	(O'Reilly and Werdell 2019)
OC5_MERIS	Blue-green ratios	MBR=Rrs(412>442>490>510)/Rrs560	0.01 to 78	(O'Reilly and Werdell 2019)
OC6_MERIS	Blue-green ratios	MBR=Rrs(412>442>490>510)/M(560&665)	0.01 to 78	(O'Reilly and Werdell 2019)
Optimized QAA for OLCI	Semi-analytical	1. Modified reference band (λ_0) of 709 or 754 nm in Step 3: $MCI = R_{rs}(709) - R_{rs}(665) - \left(R_{rs}(754) - R_{rs}(665)\right) * \frac{709-665}{754-665}$ If MCI≤0.0016, λ_0 =709 nm, else, λ_0 =754 nm 2. Modified $a_{ph}(665)$ equation and η value in step 7 $a_{ph}(665) = \eta\, a_{nw}(560) + (1-\eta)\, a_{nw}(665)$	5 to 100	(Liu, Li et al. 2020)

MDN	Machine learning	MDN	0.2 to 1209	(Pahlevan, Smith et al. 2020, Pahlevan, Smith et al. 2021, Smith, Pahlevan et al. 2021)
Bayesian	Bayesian probabilistic neural networks	BNN	0.05 to 68	(Werther, Odermatt et al. 2022)
Smith18	Switched blending (G2B and OCI)	$Chl_{blend}(mg\ m^{-3}) = \alpha_1 Chl_{G2B} + \alpha_2 Chl_{OCI}$ Where $\alpha_1 = (Ø - 0.75)/(1.15 - 0.75)$; $\alpha_2 = (1.15 - Ø)/(1.15 - 0.75)$ and Ø=$R_{rs}(708)/R_{rs}(665)$ G2B algorithm refers to Gilerson, Gitelson et al. (2010); $Chla\ [mg\ m^{-3}] = \left(A \times \left(\frac{R(709)}{R(665)}\right) + B\right)^C$ OCI algorithm refers to combined CI (Chl<0.25) and OC4E (Chl>0.25) algorithms: $CI = R_{rs}(560) - [R_{rs}(443) + (560 - 443)(665 - 443) * (R_{rs}(665) - R_{rs}(443))]$ $Chl_{CI}(mg\ m^{-3}) = 10^{(a1+b1*CI)}$ $Chl_{OC4}(mg\ m^{-3}) = 10^{(a+b\times X+c\times X^2+d\times X^3+e\times X^4)}$	0.43 to 309	(Smith, Lain et al. 2018)

Table 16 Summary of candidate new Turbidity/TSM algorithms for OLCI

Algorithm	Architectural approach	Formular	Original training (g.m-3)	reference
SOLID20	MDN-based bbp inversion	Classification based	0.1 to 2626.8	(Balasubramanian, Pahlevan et al. 2020)
Jiang21	Semi-analytical	Classification based	0.09 to 2627	(Jiang, Matsushita et al. 2021)
Novoa21G	Switch blending	Linear-Green (tsm<10): $a \times R_w(560)$ Linear-Red (tsm 10~50): $b\times R_w(665)$ Poly-NIR (tsm>50): $c \times R_w(865)^2 + d \times R_w(865)$	2.6 to 1579.1	(Novoa, Doxaran et al. 2017)
Novoa21B	Switch blending	Linear-Green (tsm<10): $a \times R_w(560)$ Nechad et al. (2010) NIR (tsm 10~50): $\frac{b\times R_w(665)}{1-R_w(665)/c}$ Nechad et al. (2010) NIR (tsm>50): $\frac{d\times R_w(865)}{1-R_w(865)/e}$	17.8 to 340.6	(Novoa, Doxaran et al. 2017)

Uudeberg20-clear	Band ratios	$logTSM = a \times R_w560 + b \times R_w665 + c \times \frac{R_w490}{R_w560} + d$	0.5 to 215.2	(Uudeberg, Aavaste et al. 2020)
Uudeberg2020-moderate	Band ratios	$TSM = a \times \left(R_w865 - \frac{R_w778.75 + R_w865}{2}\right) + b$	0.5 to 215.2	(Uudeberg, Aavaste et al. 2020)
Uudeberg20-Turbid	Band ratios	$TSM = a \times \left(R_w865 - \frac{R_w778.75 + R_w865}{2}\right) + b$	0.5 to 215.2	(Uudeberg, Aavaste et al. 2020)
Uudeberg20-VeryTurbid	Band ratios	$logTSM = a \times logR_w560 + b \times R_w665 + c \times log\frac{R_w490}{R_w560} + d$	0.5 to 215.2	(Uudeberg, Aavaste et al. 2020)
Uudeberg20-Brown	Band ratios	$lnTSM = a \times \left(R_w708.75 - \frac{R_w778.75 + R_w665}{2}\right) + b$	0.5 to 215.2	(Uudeberg, Aavaste et al. 2020)
ANTA21 (Turbidity) (based on Nechad 2009, tunned for OLCI)		T(red) was used if RW(red) < 0.05, and T(NIR) if RW(red) > 0.07, with a linear blending in the transition. Red=665 nm NIR=865 nm $T(\lambda) = \frac{A(\lambda) * R_w(\lambda)}{\frac{1 - R_w(\lambda)}{C(\lambda)}}$	0.83 to 176 FNU	(Nechad, Ruddick et al. 2009, Dogliotti, Ruddick et al. 2015, Klein, Lantuit et al. 2021)

5.2 Validation results

Prior to the Lakes_cci, extensive validation exercises were carried out on satellite-derived LWLR against in-situ remote-sensing reflectance (predominantly from above-water measurements) as well as on the retrieval of chlorophyll-a from atmospherically corrected LWLR. The number of satellite vs in-situ matchups is limited and these analyses have mostly focussed on products derived from MERIS.

5.2.1 Atmospheric correction algorithms

For LWLR, six algorithms for MERIS were initially compared: MEGS8.1 (MERIS default), FUB, CoastColour, Case2Regional, SCAPE-M and POLYMER. From these results (Figure 12 to Figure 14 give examples of MEGS and the best performing algorithms), POLYMER was selected based on its superior linearity and correlation with in-situ data despite a significant negative bias, which appears to be associated with overestimation of the atmospheric radiance component rather than the water model which is not yet well understood. Linearity in the response nevertheless suggests that algorithms for the retrieval of chlorophyll-a, total suspended matter or turbidity can be tuned to reproduce in-situ observations. This procedure is described in more detail in the E3UBv2.1.1 document.

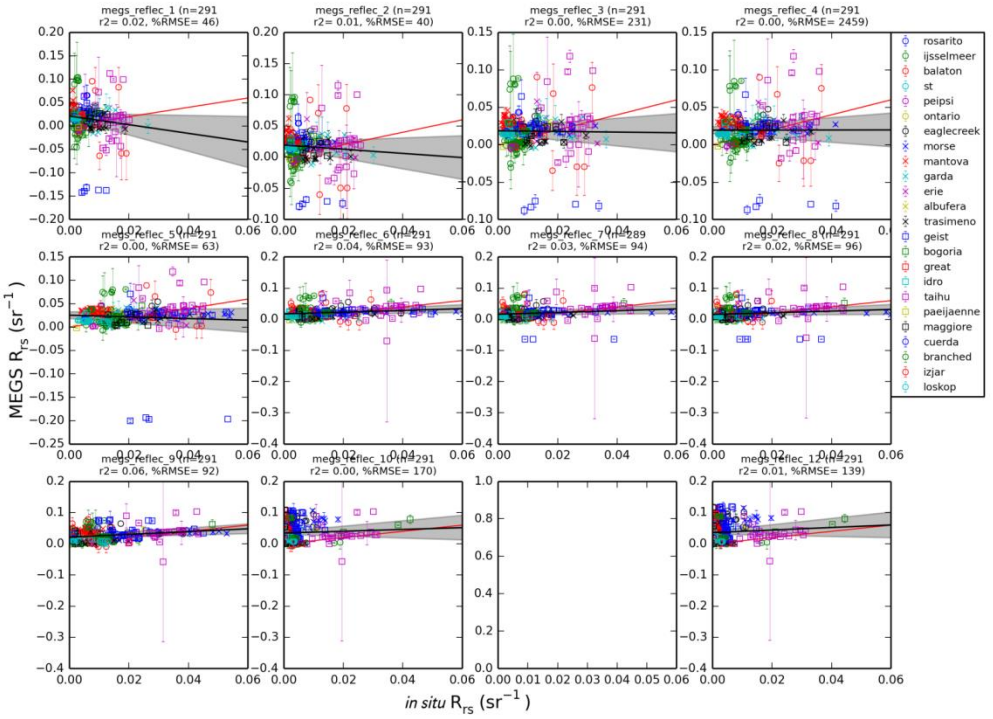

Figure 12 LWLR retrieval per MERIS waveband using the default MEGS algorithm. Matchups are for a ±7-day matchup window and 3x3 pixel extraction window and include results of 23 lakes.

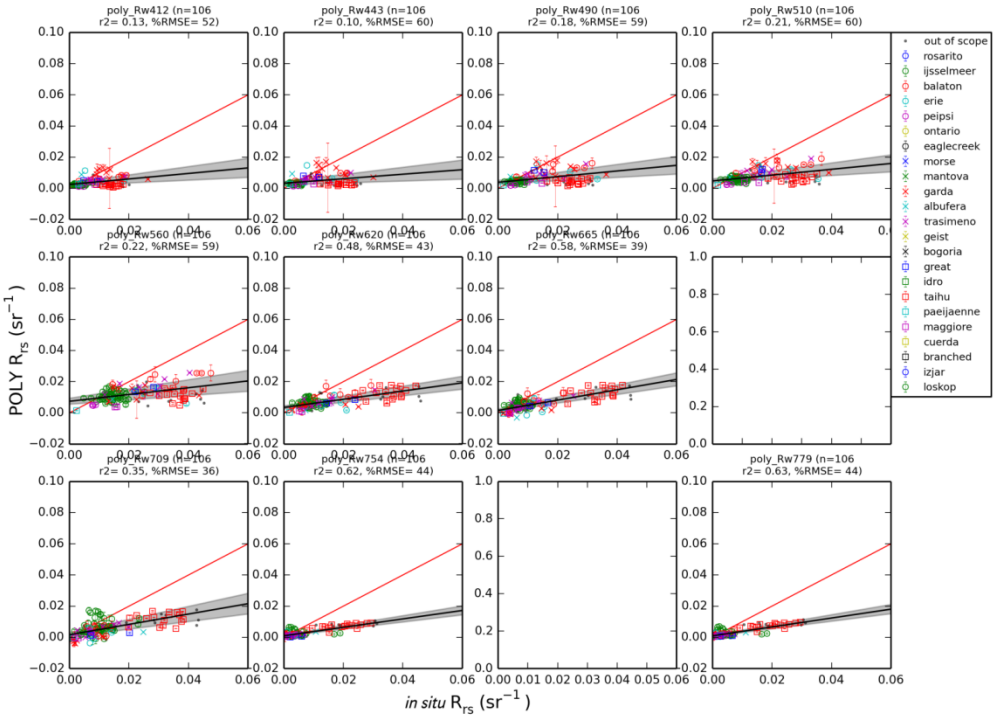

Figure 13 As previous but for the POLYMER algorithm.

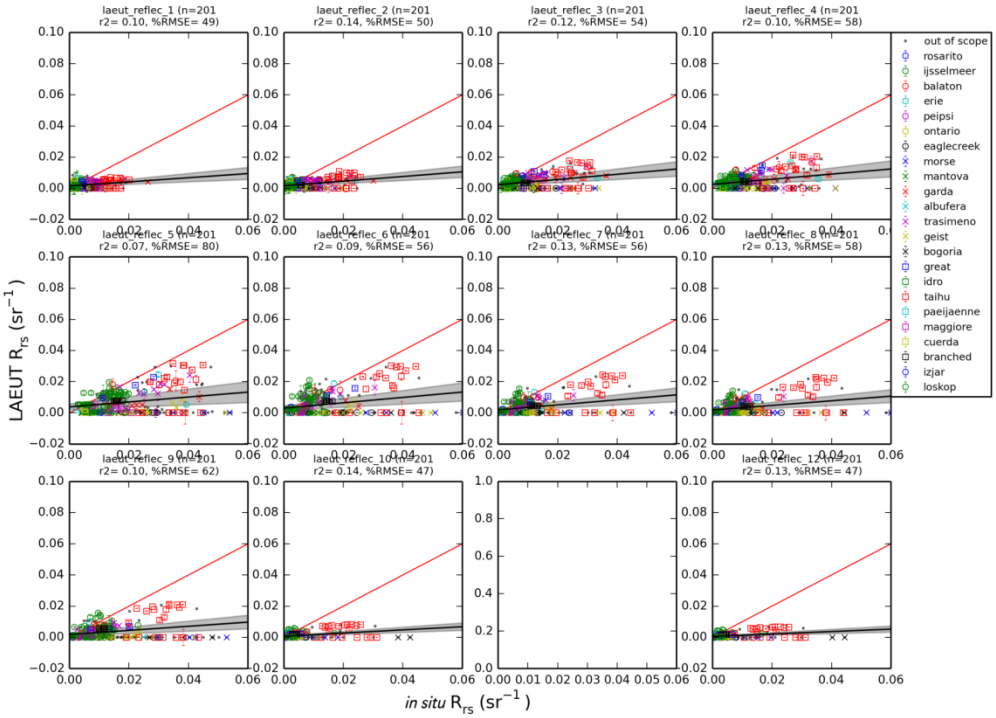

Figure 14 As previous but for the Lakes C2R algorithm.

5.2.2 Chlorophyll-a algorithms

5.2.2.1 Chlorophyll-a algorithms for MERIS

Despite higher uncertainty in the validation of LWLR due to scarce in-situ reference data, chlorophyll-a and suspended matter and/or turbidity algorithms may be evaluated and subsequently tuned based on a larger number of matchups with MERIS data in the LIMNADES data set for these measurands. Figure 15 shows results of the round-robin comparison of algorithms for chlorophyll-a, ultimately resulting in the selection of OC2, a near infra-red (NIR) over red band algorithm based on Gilerson et al. (2010), the semi-analytical NIR-red ratio algorithm of Gons et al. (2005) and a modified Quasi-Analytical Algorithm (QAA) following Mishra et al. (2013). A separate algorithm tuning exercise was also carried out using exclusively in-situ (reflectance and concentration) data, as reported by Neil et al. (2019).

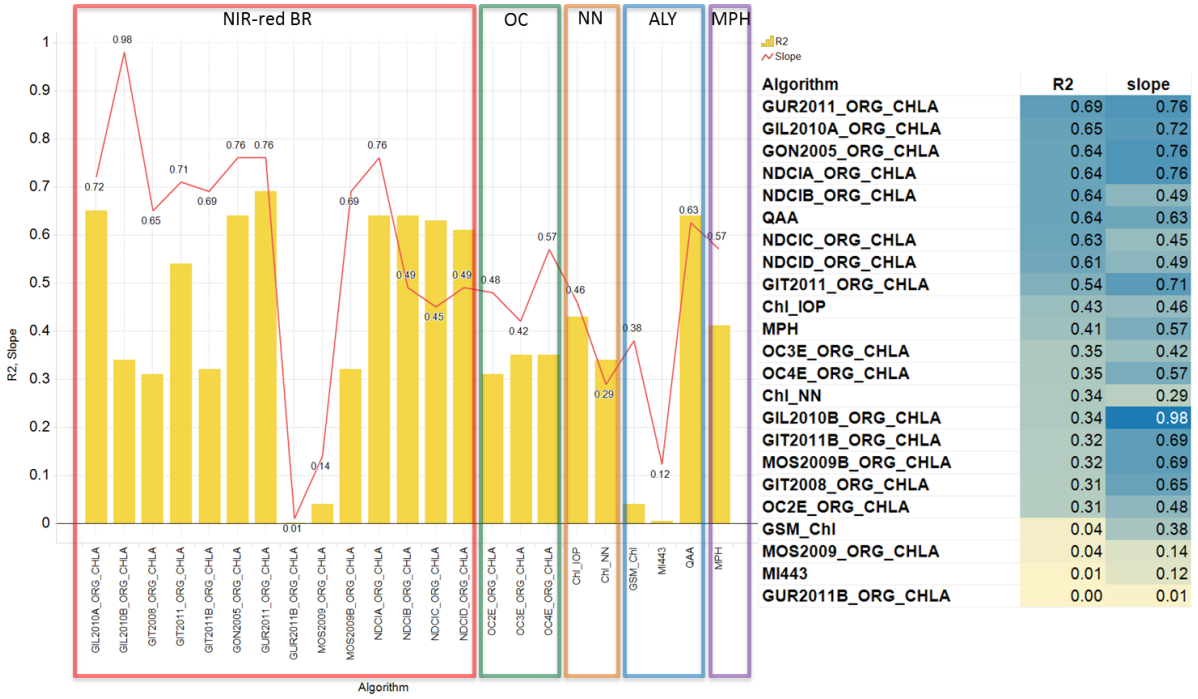

Algorithm	R2	slope
GUR2011_ORG_CHLA	0.69	0.76
GIL2010A_ORG_CHLA	0.65	0.72
GON2005_ORG_CHLA	0.64	0.76
NDCIA_ORG_CHLA	0.64	0.76
NDCIB_ORG_CHLA	0.64	0.49
QAA	0.64	0.63
NDCIC_ORG_CHLA	0.63	0.45
NDCID_ORG_CHLA	0.61	0.49
GIT2011_ORG_CHLA	0.54	0.71
Chl_IOP	0.43	0.46
MPH	0.41	0.57
OC3E_ORG_CHLA	0.35	0.42
OC4E_ORG_CHLA	0.35	0.57
Chl_NN	0.34	0.29
GIL2010B_ORG_CHLA	0.34	0.98
GIT2011B_ORG_CHLA	0.32	0.69
MOS2009B_ORG_CHLA	0.32	0.69
GIT2008_ORG_CHLA	0.31	0.65
OC2E_ORG_CHLA	0.31	0.48
GSM_Chl	0.04	0.38
MOS2009_ORG_CHLA	0.04	0.14
MI443	0.01	0.12
GUR2011B_ORG_CHLA	0.00	0.01

Figure 15 Round-robin comparison of chlorophyll-a retrieval algorithms, including NIR-red band ratio algorithms, ocean colour blue-green ratio algorithms, neural networks, analytical (multi-band) inversion algorithms and the maximum peak height algorithm.

5.2.2.2 Chlorophyll-a algorithms for MODIS

A Round-robin comparison was performed to assess the candidate Chl-a algorithms for MODIS. A total of nine algorithms were compared, including three blue-green band ratio algorithms, two NIR-red band ratio algorithms, one peak height algorithm, and two semi-analytical algorithms. Figure 16 Shows the error metrics of round-robin comparison for each evaluated Chl-a algorithm against in-situ measurements. Based on this analysis, the NASA OC2(O'Reilly et al. 1998), OC3, OC2_HI algorithms (O'Reilly et al. 1998), and R748_667 algorithm (Dall'Olmo et al. 2005) were selected for the retrieving of Chl-a for MODIS. Additionally, a separate algorithm tuning exercise was carried out using satellite and in-situ matchups for each ocean water type (OWT), taking data points within the highest 40% OWT membership scores.

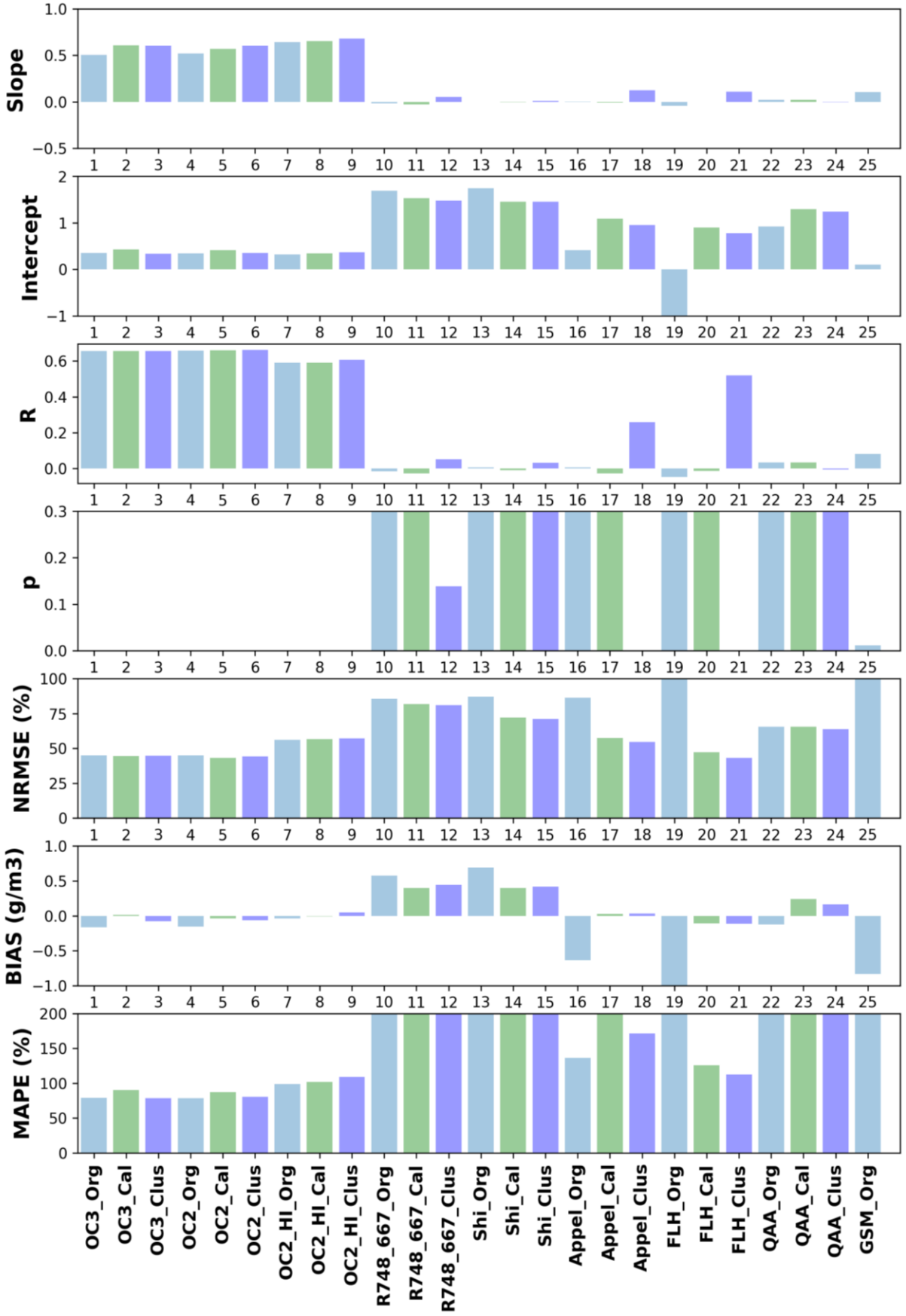

Figure 16 Statistical metrics calculated between MODIS-derived and in-situ Chl-a

5.2.3 TSM and Turbidity algorithms

5.2.3.1 TSM and Turbidity algorithms for MERIS

Algorithm comparisons for TSM and Turbidity have not yet been completed for the full set of candidate algorithms. An initial selection was made during GloboLakes based on the performance of TSM retrieval algorithms by Zhang et al. (2010), Binding et al. (2010) and Vantrepotte et al. (2011), which target different concentration ranges and optical water types. These algorithms were subsequently converted to Turbidity using the coefficients contained in the work by Nechad et al. (2010).

5.2.3.2 TSM and Turbidity algorithms for MODIS

Algorithm comparisons were performed to evaluate TSM and Turbidity for each of the examined algorithms against in-situ measurements. However, it was observed that the TSM algorithms did not exhibit satisfactory performance for MODIS measurements. As a result, the CRDP dataset does not include TSM (Turbidity) retrieval using MODIS.

5.3 Identified issues

At present, no specific validation or tuning of individual algorithms has been carried out for OLCI which instead inherits algorithms from tuning and validation for MERIS. Similarities in radiometric performance and waveband configuration between MERIS and OLCI allow us to extrapolate the current results to OLCI. Nevertheless, given the prolonged operation of OLCI and the emergence of new algorithms in recent years, a comprehensive analysis specifically tailored to OLCI is necessary. To address this, a thorough evaluation of newly published algorithms for OLCI is planned with findings to be incorporated into CRDP v3.0.

All algorithms which derive substance concentrations or turbidity from LWLRL have been tuned using water quality measurements and in-situ hyperspectral radiometric data, with the exception of MODIS-Aqua algorithms which have been tuned using LWLR derived from the satellite. It is important to acknowledge that atmospheric correction poses a significant challenge in remote estimations of water quality parameters. An analysis on Chla (Pahlevan et al. 2021) suggests that atmospheric correction can lead to a loss of performance of at least 30%. Therefore, when directly applying these algorithms to satellite data, their performance should be expected to decrease. To address this issue, it is beneficial to conduct tuning using satellite-derived reflectance. This additional tuning step aims to eliminate systematic biases introduced by the atmospheric correction procedure. By incorporating satellite-derived reflectance, the algorithms can better account for and mitigate the impact of atmospheric effects, enhancing their performance for water quality parameter estimations.

The following potential issues have been identified for the candidate algorithms to be tested for OLCI/MERIS:

Chl-a algorithms (in Table 15):

- The MDN algorithm is based on machine learning, which relies on the dataset used for training. Therefore, the performance of this algorithm is heavily dependent on the quality and representativeness of the training data. Further tuning may not be applicable for this algorithm, and validation will not be independent from the training data set.
- Similarly, the Bayesian probabilistic neural networks (BNN) method is a machine learning-based data-driven approach. Its performance is highly influenced by the dataset used for model training. The original training range of this model is designed for oligotrophic and mesotrophic lakes, and its applicability to eutrophic and hyper-eutrophic lakes is yet to be tested. Further tuning for this algorithm might not be applicable either.

- The Smith18 algorithm is a switch-blending algorithm that combines the G2B and OCI algorithms. Its performance, especially when integrated into our weighted blending procedure, still needs to be evaluated. Tuning of this algorithm should be conducted separately for the two underlying TSM/Turbidity algorithms (Table 16)
- The SOLID20 algorithm uses a classification-based approach with an MDN method for b_{bp} (particulate backscatter) retrieval. As it is based on machine learning, further tuning may not be applicable to this algorithm.
- The Novoa21G and NovoaB algorithms are both switch-blending algorithms. It is important to verify whether the outputs of these algorithms exhibit a seamless transition between the different blending modes. Additionally, each algorithm incorporated in this switch-blending approach should be individually tuned to optimize their performance.

5.4 References

Balasubramanian, S.V., Pahlevan, N., Smith, B., Binding, C., Schalles, J., Loisel, H., Gurlin, D., Greb, S., Alikas, K., & Randla, M. (2020). Robust algorithm for estimating total suspended solids (TSS) in inland and nearshore coastal waters. Remote Sens. Environ., 246: 111768

Binding, C., Bowers, D., Mitchelson-Jacob, E. (2005). Estimating suspended sediment concentrations from ocean colour measurements in moderately turbid waters; the impact of variable particle scattering properties. Rem Sens Env 94(3): 373-383.

Binding, C., Jerome, J., Bukata, R. and Booty, W. (2010). Suspended particulate matter in Lake Erie derived from MODIS aquatic colour imagery. Int J Remote Sens 31(19).

Boss, E. and Roesler C. (2006). Over Constrained Linear Matrix Inversion with Statistical Selection. *In:* Lee, ZP (Ed.), IOCCG Report nr 5. Remote Sensing of Inherent Optical Properties: Fundamentals, Tests of Algorithms, and Applications., pp. 126.

Carder KL, Chen FR, Cannizzaro JP, et al (2004) Performance of the MODIS semi-analytical ocean color algorithm for chlorophyll-a. Adv Space Res 33:1152–1159.

Chen S, Han L, Chen X, et al (2015) Estimating wide range Total Suspended Solids concentrations from MODIS 250-m imageries: An improved method. ISPRS J Photogramm Remote Sens 99:58–69.

Chen Z, Hu C, Muller-Karger F (2007) Monitoring turbidity in Tampa Bay using MODIS/Aqua 250-m imagery. Remote Sens Environ 109:207–220.

Constantin S, Constantinescu Ștefan, Doxaran D (2017) Long-term analysis of turbidity patterns in Danube Delta coastal area based on MODIS satellite data. J Marine Syst 170:10–21.

Dall'Olmo G, Gitelson AA, Rundquist DC, et al (2005) Assessing the potential of SeaWiFS and MODIS for estimating chlorophyll concentration in turbid productive waters using red and near-infrared bands. Remote Sens Environ 96:176–187.

Dekker, A. Vos, R., Peters, S. (2002). Analytical algorithms for lake water TSM estimation for retrospective analyses of TM and SPOT sensor data, Int J Rem Sens 23(1):15-35.

Dogliotti, A.I., Ruddick, K., Nechad, B., Doxaran, D., & Knaeps, E. (2015). A single algorithm to retrieve turbidity from remotely-sensed data in all coastal and estuarine waters. Remote Sens. Environ., 156: 157-168

Doxaran D, Froidefond J-M, Castaing P, Babin M (2009) Dynamics of the turbidity maximum zone in a macrotidal estuary (the Gironde, France): Observations from field and MODIS satellite data. Estuar Coastal Shelf Sci 81:321–332.

D'Sa, E. , Miller, R., McKee, B. (2007). Suspended particulate matter dynamics in coastal waters from ocean color: Application to the northern Gulf of Mexico, Geophys Res Lett 34, L23611.

El-Alem A, Chokmani K, Laurion I, El-Adlouni SE (2012) Comparative Analysis of Four Models to Estimate Chlorophyll-a Concentration in Case-2 Waters Using MODerate Resolution Imaging Spectroradiometer (MODIS) Imagery. Remote Sens 4:2373–2400.

Eleveld, M., Pasterkamp, R., Van der Woerd, H., Pietrzak, J. (2008). Remotely sensed seasonality in the spatial distribution of sea-surface suspended particulate matter in the southern North Sea. Est Coast Shelf Sci 80(10): 103-113.

Gilerson, A., Gitelson, A., Zhou, J., Gurlin, D., Moses, W., Ioannou, I. and Ahmed, S. (2010). Algorithms for remote estimation of chlorophyll-a in coastal and inland waters using red and near infrared bands. Opt Express 18(23): 24109-24125.

Gitelson A (1992) The peak near 700 nm on radiance spectra of algae and water: relationships of its magnitude and position with chlorophyll concentration. Int J Remote Sens 13:3367–3373

Gitelson AA, Schalles JF, Hladik CM (2007) Remote chlorophyll-a retrieval in turbid, productive estuaries: Chesapeake Bay case study. Remote Sens Environ 109:464–472.

Gitelson, A., Dall'Olmo, G., Moses, W., Rundquist, D., Barrow, T., Fisher, T., Gurlin, D., Holz, J. (2008). A simple semi-analytical model for remote estimation of chlorophyll-a in turbid waters: Validation. Remote Sens Environ 112 (9), 3582–3593.

Gitelson, A., Gurlin, D., Moses, W., Yacobi, Y. (2011). Remote estimation of Chlorophyll-a concentration in inland, estuarine, and coastal waters. *In*: Weng, Q. (Ed.), Advances in Environmental Remote Sensing: Sensors, Algorithms, and Applications. CRC Press, Taylor and Francis Group, pp. 449–478 (610 p. ISBN: 9781420091755).

Gons H., Rijkeboer M., Ruddick K. (2005). Effect of a waveband shift on chlorophyll retrieval from MERIS imagery of inland and coastal waters. J Plankton Res 27(1):125-7.

Guanter L, Del Carmen González-Sanpedro M, Moreno J (2007) A method for the atmospheric correction of ENVISAT/MERIS data over land targets. Int J Remote Sens 28:709–728

Gurlin, D., Gitelson, A., Moses, W. (2011). Remote estimation of chl-a concentration in turbid productive waters — return to a simple two-band NIR-red model? Remote Sens Environ 115 (12), 3479–3490.

Ha N, Koike K, Nhuan M (2013) Improved Accuracy of Chlorophyll-a Concentration Estimates from MODIS Imagery Using a Two-Band Ratio Algorithm and Geostatistics: As Applied to the Monitoring of Eutrophication Processes over Tien Yen Bay (Northern Vietnam). Remote Sens 6:421–442.

Ioannou, I., Gilerson, A., Gross, B., Moshary, F., Ahmed, S. (2013). Deriving ocean color products using neural networks. Remote Sens Environ 134, 78e91.

Jiang, D., Matsushita, B., Pahlevan, N., Gurlin, D., Lehmann, M.K., Fichot, C.G., Schalles, J., Loisel, H., Binding, C., & Zhang, Y. (2021). Remotely estimating total suspended solids concentration in clear to extremely turbid waters using a novel semi-analytical method. Remote Sens. Environ., 258: 112386

Klein, K.P., Lantuit, H., Heim, B., Doxaran, D., Juhls, B., Nitze, I., Walch, D., Poste, A., & Søreide, J.E. (2021). The Arctic Nearshore Turbidity Algorithm (ANTA)-A multi sensor turbidity algorithm for Arctic nearshore environments. Science of Remote Sensing, 4: 100036

Lee Z, Carder KL, Arnone RA (2002) Deriving inherent optical properties from water color: a multiband quasi-analytical algorithm for optically deep waters. Appl Opt 41:5755–5772

Lehmann, M.K., Gurlin, D., Pahlevan, N. et al. (2023). GLORIA - A globally representative hyperspectral in-situ dataset for optical sensing of water quality. Sci Data 10, 100 (2023). https://doi.org/10.1038/s41597-023-01973-y

Letelier R (1996) An analysis of chlorophyll fluorescence algorithms for the moderate resolution imaging spectrometer (MODIS). Remote Sens Environ 58:215–223.

Liu, G., Li, L., Song, K., Li, Y., Lyu, H., Wen, Z., Fang, C., Bi, S., Sun, X., & Wang, Z. (2020). An OLCI-based algorithm for semi-empirically partitioning absorption coefficient and estimating chlorophyll a concentration in various turbid case-2 waters. Remote Sens. Environ., 239: 111648

Loisel, H., Mangin, A., Vantrepotte, V., Dessailly, D., Dinh, D. N., Garnesson, P. Ouillon, S., Lefebvre, J. P., Mériaux, X., Phan, T. M. (2014). Variability of suspended particulate matter concentration in coastal waters under the Mekong's influence from ocean color (MERIS) remote sensing over the last decade. Rem Sens Environ 150: 218-230.

Maritorena, S., Siegel, D., Peterson, A. (2002). Optimization of a semianalytical ocean color model for global-scale applications. Appl Opt 41, 2705–2714.

Matthews, M., Bernard, S., Robertson, L. (2012). An algorithm for detecting trophic status (chlorophyll-a), cyanobacterial-dominance, surface scums and floating vegetation in inland and coastal waters. Remote Sens Environ 124, 637–652.

Miller RL, McKee BA (2004) Using MODIS Terra 250 m imagery to map concentrations of total suspended matter in coastal waters. Remote Sens Environ 93:259–266.

Mishra S., Mishra D., Lee Z. (2014). Bio-optical inversion in highly turbid and cyanobacteria-dominated waters. (2014): IEEE Trans Geosci Remote Sens 52(1):375-88.

Mishra, S., Mishra, D. (2012). Normalized difference chlorophyll index: a novel model for remote estimation of chlorophyll-a concentration in turbid productive waters. Remote Sens Environ 117, 394–406.

Moreno-Madrinan MJ, Al-Hamdan MZ, Rickman DL, Muller-Karger FE (2010) Using the Surface Reflectance MODIS Terra Product to Estimate Turbidity in Tampa Bay, Florida. Remote Sens 2:2713–2728.

Moses, W., Gitelson, A., Berdnikov, S., Povazhnyy, V. (2009). Satellite estimation of chlorophyll-a concentration using the red and NIR bands of MERIS — the Azov Sea case study. IEEE Geosci Remote Sens Lett. 6 (4), 845–849.

Nechad, B., Dogliotti, A. I., Ruddick, K. G., Doxaran, D. (2016). Particulate Backscattering and suspended matter concentration retrieval from remote-sensed turbidity in various coastal and riverine turbid waters. Proceedings of ESA Living Planet Symposium, Prague, 9-13 May 2016, ESA-SP 740.

Nechad, B., Ruddick, K., & Neukermans, G. (2009). Calibration and validation of a generic multisensor algorithm for mapping of turbidity in coastal waters. In, Remote Sensing of the Ocean, Sea Ice, and Large Water Regions 2009 (pp. 161-171): SPIE

Nechad, B., Ruddick, K., Park, Y. (2010). Calibration and validation of a generic multisensor algorithm for mapping of total suspended matter in turbid waters". Remote Sens Environ 114 (2010) 854–866.

Neil, C., Spyrakos, E., Hunter, P., Tyler, A. (2019). A global approach for chlorophyll-a retrieval across optically complex inland waters based on optical water types. Remote Sens Environ 229: 159-178.

Novoa, S., Doxaran, D., Ody, A., Vanhellemont, Q., Lafon, V., Lubac, B., & Gernez, P. (2017). Atmospheric corrections and multi-conditional algorithm for multi-sensor remote sensing of suspended particulate matter in low-to-high turbidity levels coastal waters. Remote Sens., 9(1): 61

O'Reilly, J, Maritorena, S., O'brien, M., Siegel, D., Toole, D., Menzies, D., Smith, R. et al. (2000). SeaWiFS postlaunch calibration and validation analyses, part 3. NASA tech. memo 206892, no. 11 (2000): 3-8.

Ondrusek M, Stengel E, Kinkade CS, et al (2012) The development of a new optical total suspended matter algorithm for the Chesapeake Bay. Remote Sens Environ 119:243–254.

O'Reilly, J.E., & Werdell, P.J. (2019). Chlorophyll algorithms for ocean color sensors-OC4, OC5 & OC6. Remote Sens. Environ., 229: 32-47

Pahlevan, N., Smith, B., Binding, C., Gurlin, D., Li, L., Bresciani, M., & Giardino, C. (2021). Hyperspectral retrievals of phytoplankton absorption and chlorophyll-a in inland and nearshore coastal waters. Remote Sens. Environ., 253: 112200

Pahlevan, N., Smith, B., Schalles, J., Binding, C., Cao, Z., Ma, R., Alikas, K., Kangro, K., Gurlin, D., & Hà, N. (2020). Seamless retrievals of chlorophyll-a from Sentinel-2 (MSI) and Sentinel-3 (OLCI) in inland and coastal waters: A machine-learning approach. Remote Sens. Environ., 240: 111604

Petus C, Chust G, Gohin F, et al (2010) Estimating turbidity and total suspended matter in the Adour River plume (South Bay of Biscay) using MODIS 250-m imagery. Cont Shelf Res 30:379–392.

Polito CD, Di Polito C, Ciancia E, et al (2016) On the Potential of Robust Satellite Techniques Approach for SPM Monitoring in Coastal Waters: Implementation and Application over the Basilicata Ionian Coastal Waters Using MODIS-Aqua. Remote Sens 8:922.

Robert E, Grippa M, Kergoat L, et al (2016) Monitoring water turbidity and surface suspended sediment concentration of the Bagre Reservoir (Burkina Faso) using MODIS and field reflectance data. Int J Appl Earth Obs. 52:243–251.

Ruddick KG, Ovidio F, Rijkeboer M (2000) Atmospheric correction of SeaWiFS imagery for turbid coastal and inland waters. Appl Opt 39:897–912.

Smith, B., Pahlevan, N., Schalles, J., Ruberg, S., Errera, R., Ma, R., Giardino, C., Bresciani, M., Barbosa, C., & Moore, T. (2021). A chlorophyll-a algorithm for Landsat-8 based on mixture density networks. Frontiers in Remote Sensing, 1: 623678

Smith, M.E., Lain, L.R., & Bernard, S. (2018). An optimized chlorophyll a switching algorithm for MERIS and OLCI in phytoplankton-dominated waters. Remote Sens. Environ., 215: 217-227

Spyrakos E, O'Donnell R, Hunter PD, Miller C, Scott M, Simis S, et al. (2018). Optical types of inland and coastal waters. Limnol Oceanogr. 63(2).

Uudeberg, K., Aavaste, A., Kõks, K.-L., Ansper, A., Uusõue, M., Kangro, K., Ansko, I., Ligi, M., Toming, K., & Reinart, A. (2020). Optical water type guided approach to estimate optical water quality parameters. Remote Sens., 12(6): 931

Werther, M., Odermatt, D., Simis, S.G., Gurlin, D., Lehmann, M.K., Kutser, T., Gupana, R., Varley, A., Hunter, P.D., & Tyler, A.N.J.R.S.o.E. (2022). A Bayesian approach for remote sensing of chlorophyll-a and associated retrieval uncertainty in oligotrophic and mesotrophic lakes, 283: 113295

6 Lake Ice cover – LIC

6.1 Candidate algorithms

Four machine learning (ML) algorithms were evaluated for their performance in classifying lake ice cover, open water and cloud cover: multinomial logistic regression (MLR), support vector machine (SVM), random forest (RF), and gradient boosting trees (GBT). The characteristics of each ML algorithm are summarized below. Full details, including the hyperparameters used by each classifier, can be found in Wu et al. (2021).

Multinomial logistic regression (MLR). MLR is an extension of logistic regression applied to multiple response variables. Logistic regression is used as an approach to develop a model of the log odds of binary class probabilities as a linear function of one or more explanatory variables (Murphy, 2013). Then, the model can inversely compute the probability of each class using the explanatory variables of a given unknown sample. Specifically, in order to tackle multi-class problem, MLR designates one of the response variables as the baseline class. In this manner, the probability of membership in the different classes is related to the probability of membership in the baseline class. The optimal values of the function parameters are computed using the training data. The MLR probability estimate for each class falls within a range from 0 to 1, resulting in a realistic probability surface. The maximum probability among the classes is the predicted class for an unknown sample.

Support vector machine (SVM). SVM's basic idea is to determine support vectors to build an optimal boundary separating the given observations in terms of classes (Burges, 1998; Vapnik, 1998; Weston & Watkins, 1999). The distance from the support vectors to a hyperplane is known as the margin. SVM, in its simplest form, is a linear binary classifier that labels a given sample using a hyperplane in the original input space. However, to solve the inseparability problem in the original space, SVM maps multidimensional data into an enlarged feature space to build a hyperplane using a kernel function (e.g., polynomial, radial basis, sigmoid). Since the radial basis function (RBF) kernel has a promising ability in non-linear classification, and as shown in several recent studies (Féret et al., 2019; Ge et al., 2018; Huang et al., 2019; Tian et al., 2020), the RBF kernel was adopted in this research over the linear kernel. We applied the one-vs-one scheme to handle the multiclass problem. SVM is sometimes called a soft margin classifier because training samples could lie on the incorrect side of the hyperplane, thereby creating a violation. The model hyperparameter, *Cost*, is a regularization constant controlling the violation degree. Another model hyperparameter, *Gamma*, is the kernel width of RBF.

Random forest (RF). As an ensemble approach, RF integrates decision trees developed by bagging samples to improve the limitations of the single-tree structure (Breiman, 2001). The bagging creates several subsets randomly from training samples with replacement (i.e. a sample can be collected several times in the same subset whereas other samples are probably not selected in this subset). Subsequently, each data subset is used to train a decision tree. For building a single tree, a random sample with a number of variables is chosen as split candidates from all variables. The number of variables available to a split is one of key RF hyperparameters, denoted as *mtry*. For the whole RF model, the number of trees (*ntree*) is defined *a priori* to develop various independent classifier outputs. The final class of each unknown sample is assigned by the majority vote of all outputs from the trees.

Gradient boosting trees (GBT). GBT is another ensemble classifier inspired by the boosting technique developed by Freund and Schapire (1996). In contrast to RF, GBT applies the entire training dataset on classification rather than resampling partial samples. The training samples are initially assigned equal weights in the first iteration to develop the first tree, and afterwards the weights are altered based on the fitting performance to the training dataset. Misclassified samples in the previous iteration are assigned a higher weight in subsequent iterations. Each tree is also given a weight based on the fitting error. The

final class of an unknown observation is assigned by computing the output of all trees multiplied by their weights. The term, gradient, is associated with iterative functional gradient descent algorithms used to optimize cost functions. Similar to RF, the hyperparameters of GBT, as a tree-based classifier, include the number of variables available to a split (*mtry*) and the number of trees (or iterations) (*ntree*). Moreover, an additional hyperparameter, learning rate (*lr*), controls overfitting in the range between 0 and 1 via shrinkage. The higher *lr* drives a faster learning process, and vice versa.

The candidate algorithm retained for the retrieval of LIC is the RF classifier. RF was found to outperform MLR and SVM, and comparable to GBT for lake ice cover, open water and cloud classification. While RF and GBT provided similar results following a comprehensive accuracy assessment (cross validation (CV): random k-fold as well as spatial and temporal CV), the former was selected for LIC product generation since it was determined to be less sensitive to the to the choice of hyperparameters necessary for classification compared to GBT, MLR and SVM. Validation results that support the selection of the RF classifier for Lakes_cci LIC product generation are provided below.

6.2 Validation results

To identify the best classifier, 17 lakes distributed across the Northern Hemisphere were selected (Figure 17 and Table 17). Training, testing and validation of the four machine learning algorithms found that RF with a combination of visible, near infrared, and mid infrared bands was the best choice for LIC product (Figure 18). More specifically, six MODIS (Terra/Aqua) TOA reflectance bands and the solar zenith angle (SZA) are used for feature retrieval (i. e. for labelling as water, ice, or cloud) (Wu et al., 2021). The reflectance bands are MOD02QKM/MYD02QKM at 250 m (band 1: 0.645 µm and band 2: 0.858µm) and MOD02HKM/MYD02HKM at 500 m (band 3: 0.469µm; band 4: 0.555µm; band 6: 1.640 µm; band 7: 2.130 µm) resolutions. Geolocation is provided at 1 km resolution and is interpolated to 250 m.

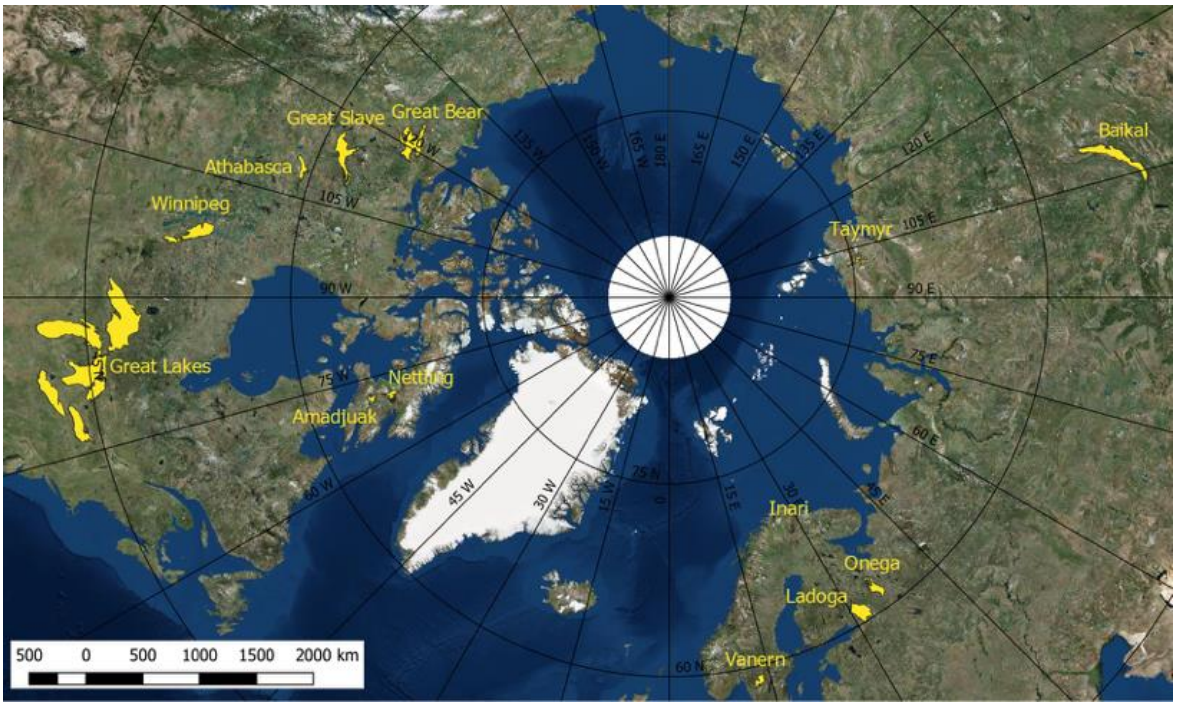

Figure 17 Geographical distribution of lakes used for LIC algorithm development and validation

Table 17 List of lakes for LIC algorithm development and (internal) validation

Lake	Country	Latitude	Longitude	Elevation (m)	Area (km²)
Amadjuak	Canada	64.925	-71.149	113	3,115
Athabasca	Canada	59.424	-109.34	213	7,900
Baikal	Russia	53.525	108.207	456	31,500
Erie	Canada/USA	42.209	-81.246	174	25,821
Great Bear	Canada	66.024	-120.61	186	31,153
Great Slave	Canada	61.579	-114.196	156	28,568
Huron	Canada/USA	44.918	-82.455	176	59,570
Inari	Finland	69.048	27.876	118	1,040
Ladoga	Russia	60.83	31.578	5	18,135
Michigan	USA	43.862	-87.093	177	58,016
Nettilling	Canada	66.42	-70.28	30	5,542
Onega	Russia	61.75	35.407	35	9,890
Ontario	Canada/USA	43.636	-77.727	75	19,009
Superior	Canada/USA	47.945	-87.32	183	82,367
Taymyr	Russia	74.538	101.639	6	4,560
Vanern	Sweden	58.88	13.22	44	5,650
Winnipeg	Canada	52.421	-97.677	217	23,750

Figure 19 shows the accuracies computed from a 100-fold cross-validation (CV) using the samples of MODIS Terra from the 17 lakes. Random forest (RF) was found to outperform MLR and SVM and comparable to GBT for lake ice cover, open water and cloud classification in a paper by the developers of the current LIC product (Wu et al. 2021). Furthermore, RF provided consistent results based on a comprehensive accuracy assessment (random k-fold as well as spatial and temporal CV as shown in

Table *18*).

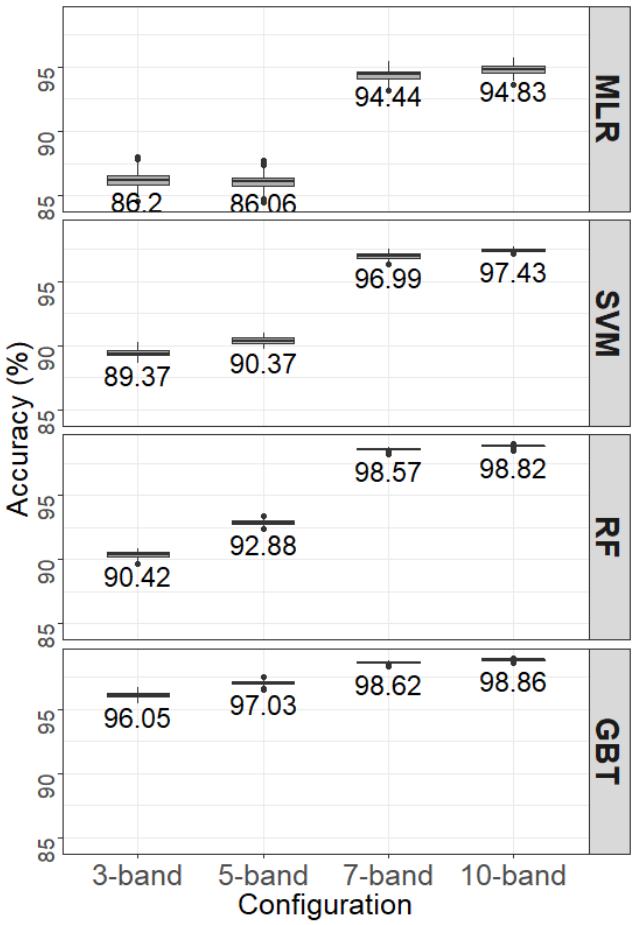

Figure 18 Comparison of classification accuracies (%) obtained with different band configurations across classifiers. The 7-band combination using RF is the one retained for generation of the LIC v2.1 product (Wu et al., 2021)

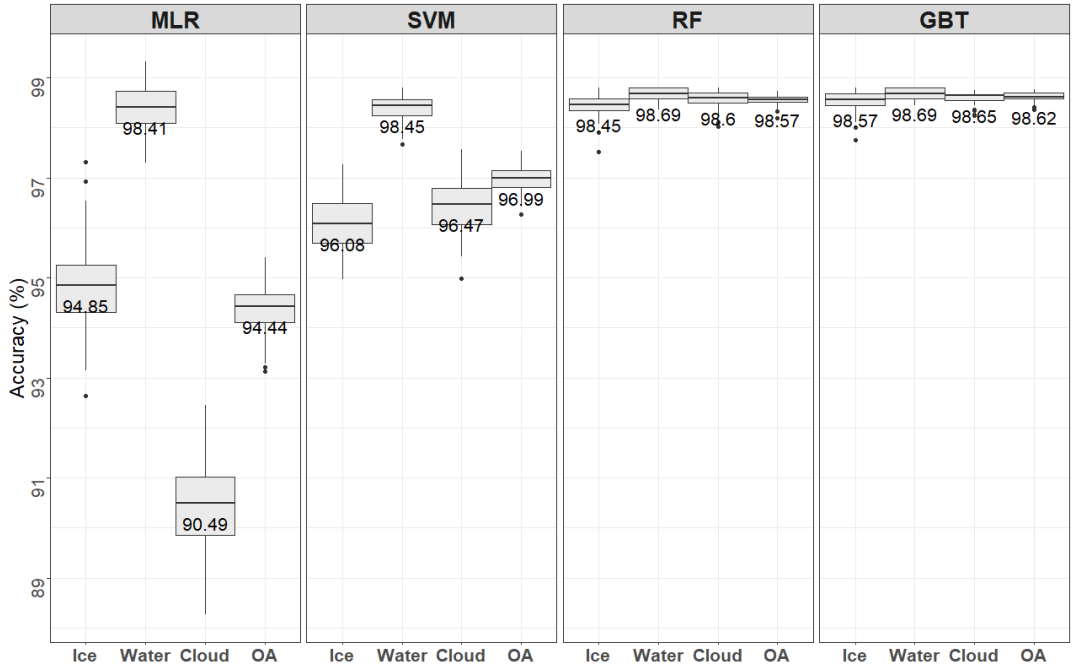

Figure 19 Comparison of accuracies (%) obtained using random 100-fold CV across classifiers for the ice, water and cloud classes individually, and overall (OA) (Wu et al., 2021)

Table 18 Accuracy assessment using temporal and spatial CV methods (adapted from Wu et al., 2021)

	MLR	SVM	RF	GBT
Temporal CV accuracy	93.21%	83.00%	95.49%	95.15%
Spatial CV accuracy	90.98%	79.36%	95.64%	95.26%

6.3 Identified issues

The RF classifier was selected for LIC product generation since it has been shown to outperform threshold-based approaches (as determined during the early stages of Lakes_cci Phase 1) and the other machine learning classifiers as presented in the previous section. While high overall accuracies (>95%) has been achieved with the RF classifier in both spatial and temporal transferability assessments (Wu et al., 2021), visual assessment of CRDP v2.1 LIC product quality over many lakes during both the ice freeze-up and break-up periods has revealed the need to collect more training and test sites to further improved product quality for future releases.

As with any lake product generated from optical data, the presence of clouds as well as extensive cloud cover periods and low solar illumination angles, particularly during the fall freeze-up at high latitudes, introduce classification errors and limit the retrieval of open water and ice cover for many days of the year. In CRDP v2.1, highly turbid lakes or sections of lakes have been found to occasionally be misclassified as ice-covered during the open water season. This is also the case for a few lakes that are characterized by snow-free "blue" clear ice during spring break-up; here ice is misclassified as open water.

One limitation of the LIC product is that no retrieval is performed when the solar zenith angle is >85 degrees; a limitation due to the use of MODIS shortwave bands that record very low surface reflectance during ice formation late fall and wintertime. Work is underway to reduce the classification errors described above through the collection of additional training sites at lake locations where misclassification (turbid water as ice cover and melting blue clear ice as open water) has been found to occur. Uncertainty is currently being reported has overall classification error for each class (water, ice, clouds). Improved classification accuracy and provision of per-pixel uncertainty (aleatoric, systematic and total) estimates are planned for CRDP v3.0.

6.4 References

Breiman, L. (2001). Random forests. Machine Learning, 45(1), 5–32. https://doi.org/10.1023/A:1010933404324.

Burges, C. J. C. (1998). A tutorial on support vector machines for pattern recognition. *Data Mining and Knowledge Discovery*, *2*(2), 121–167. https://doi.org/10.1023/A:1009715923555

Féret, J. -., le Maire, G., Jay, S., Berveiller, D., Bendoula, R., Hmimina, G., . . . Lefèvre-Fonollosa, M. -. (2019). Estimating leaf mass per area and equivalent water thickness based on leaf optical properties: Potential and limitations of physical modeling and machine learning. *Remote Sensing of Environment*, 231, doi:10.1016/j.rse.2018.11.002

Freund, Y., & Schapire, R. E. (1996). Experiments with a new boosting algorithm. In *International Conference on Machine Learning* (pp. 148–156). Retrieved from http://citeseerx.ist.psu.edu/viewdoc/summary?doi=10.1.1.51.6252

Ge, J., Meng, B., Liang, T., Feng, Q., Gao, J., Yang, S., . . . Xie, H. (2018). Modeling alpine grassland cover based on MODIS data and support vector machine regression in the headwater region of the Huanghe river, China. *Remote Sensing of Environment*, 218, 162-173. doi:10.1016/j.rse.2018.09.019

Huang, X., Liao, C., Xing, M., Ziniti, B., Wang, J., Shang, J., . . . Torbick, N. (2019). A multi-temporal binary-tree classification using polarimetric RADARSAT-2 imagery. *Remote Sensing of Environment*, 235, doi:10.1016/j.rse.2019.111478

Murphy, K. P. (2013). *Machine learning : a probabilistic perspective*. Cambridge, Mass. [u.a.]: MIT Press. Retrieved from https://www.amazon.com/Machine-Learning-Probabilistic-Perspective-Computation/dp/0262018020/ref=sr_1_2?ie=UTF8&qid=1336857747&sr=8-2

Tian, J., Wang, L., Yin, D., Li, X., Diao, C., Gong, H., . . . Liu, X. (2020). Development of spectral-phenological features for deep learning to understand spartina alterniflora invasion. *Remote Sensing of Environment*, 242, doi:10.1016/j.rse.2020.111745

Vapnik, V. (1998). The Support Vector Method of Function Estimation. In J. A. K. Suykens & J. Vandewalle (Eds.), *Nonlinear Modeling: Advanced Black-Box Techniques* (pp. 55–85). Boston, MA: Springer US. https://doi.org/10.1007/978-1-4615-5703-6_3

Weston, J., & Watkins, C. (1999). Support vector machines for multi-class pattern recognition. *Proceedings of the 7th European Symposium on Artificial Neural Networks (ESANN-99)*, (April), 219–224.

Wu, Y., Duguay, C.R. & Xu, L. (2021). Assessment of machine learning classifiers for global lake ice cover mapping from MODIS TOA reflectance data. *Remote Sensing of Environment*, 253, 112206, https://doi.org/10.1016/j.rse.2020.112206.

7 Lake Ice Thickness- LIT

7.1 Candidate algorithms

Few studies have investigated the potential of satellite remote sensing data for the estimation of LIT to date. Kang et al. (2010) first showed that brightness temperature (Tb) measurements from the Advanced Microwave Scanning Radiometer for EOS (AMSR-E) at 18.7 GHz frequency (V polarization) to be highly sensitive (R2 = 0.91) to the seasonal evolution of ice thickness on Great Bear Lake (GBL) and Great Slave Lake (GSL), Canada. Based on this finding, Kang et al 2014 proposed empirical (linear regression) equations to estimate LIT for the two lakes using 18.7 GHz V-pol data (2002-2009), achieving a mean bias error (MBE) of 0.06 m and root mean square error (RMSE) of 0.19 m when compared to in-situ measurements. Surface temperature observations of snow-covered lake ice from the Moderate Resolution Imaging Spectroradiometer (MODIS) have also been assessed for the estimation of LIT. Using heat balance terms and snow depth derived from the Canadian Lake Ice Model (CLIMo, Duguay et al. 2003), Kheyrollah et al. (2017) retrieved ice thicknesses up to ~ 1.2 m from MODIS (2002-2014) with an RMSE of 0.17 m and MBE of 0.07 m when comparing LIT values from single pixels (1 km x 1 km) to those from close by near-shore field measurements collected on GSL and Baker Lake, Canada. Beckers et al. (2017) analysed waveforms from CryoSat2 (CS2) Ku-band synthetic aperture radar (SAR) altimetry for the estimation of LIT on the Great Bear Lake and Great Slave Lake. By exploiting the increasing distance between peak radar returns from the snow-ice and ice-water interfaces on the leading edge of waveforms with ice growth, the authors estimated ice thickness empirically with RMSE < 0.33 m when compared to in-situ measurements from the same near-shore location on GSL as in previous investigations. While data from CS2 show strong potential for the retrieval of LIT, the drifting orbit of the satellite makes it difficult to build a geographically precise time series of LIT measurements (i.e. repeated along the same tracks over the lifetime of the satellite) required for climate monitoring. Also, the LIT retracker algorithm developed in Beckers et al. (2017) relies on the empirical thresholding of the radar waveforms that is hard to generalize to follow the LIT evolution, in particular at the seasonal transitions, and can lead to biases and sub-optimal LIT estimates. More recent studies (e.g., Shu et al., 2020; Yang et al., 2021), have estimated LIT with radar altimetry data, more specifically from Sentinel-3 and Jason-3 missions, in the context of lake water level analysis, as the presence of lake ice has been shown to introduce a bias on winter water level measurements. These studies also used empirical methods based on already existing retrackers that are not specifically designed for the estimation of LIT. To overcome these limitations, Mangilli et al. (2022) developed a novel physically-based retracking algorithm, the LRM_LIT retracker, founded on the exploitation of the Ku band radar waveforms data in Low Resolution Mode (LRM) specifically tailored for the retrieval of LIT. The advantage of a physically-based and analytical retracker is that it does not rely on empirical or by-hand settings, allowing to derive robust and continuous LIT estimates over different target lakes and LRM radar altimetry missions, making the LRM_LIT algorithm the suitable tool to build robust and long LIT timeseries for climate monitoring. The LRM_LIT retacker is the algorithm currently being implemented in the lakes_cci LIT processor.

7.2 Validation results

The validation results of the selected LRM_LIT retracker algorithm are presented in detail in Mangilli et al. (2022) and are also described in the ATBD v2.1.1, E3UB v2.1.1 and PVP v2.1.1 documents.

The LRM_LIT retracker retained for the generation of the LIT product has been validated on simulations representative of Jason-like missions over Great Slave Lake. A summary is given in Figure 20, where the top plots refer to winter-like simulated waveforms (left panel) and the LIT histogram (right panel).

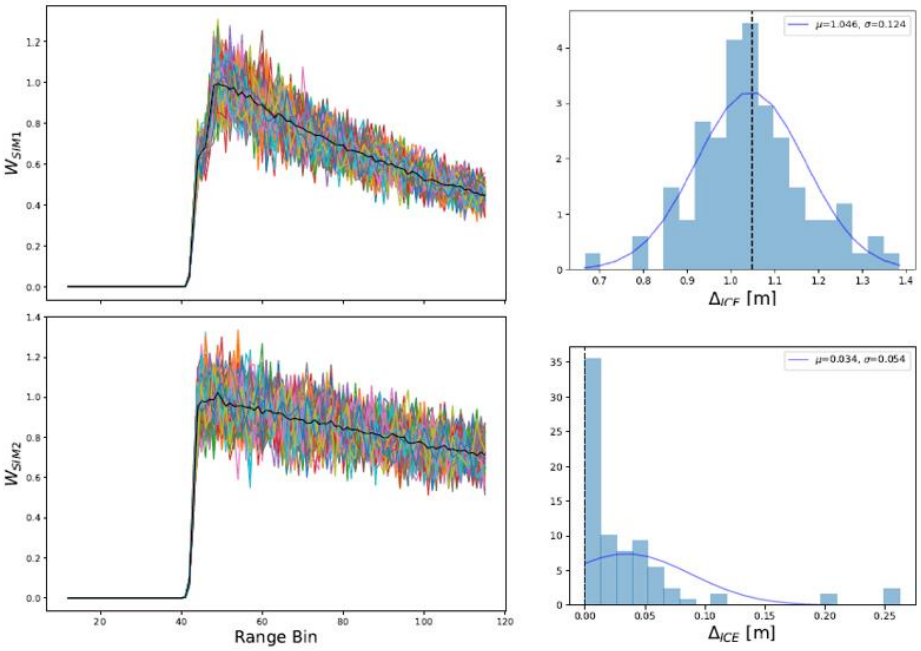

Figure 20: Validation of the LIT estimation with the LRM_LIT retracker on Jason-like simulations. In the left column are shown Jason-like waveform simulations corresponding to the winter-like SIM1 waveforms (top) and to the summer-like SIM2 waveforms. In the right column are shown LIT histograms computed for the winter-like simulations SIM1 (top panel) and for the summer-like simulations SIM2 (bottom panel). The blue lines correspond to the Gaussian fit of the histograms. The input values used to generate the simulations are also shown as dashed black lines

The input value used to generate the simulations is shown as a dashed line. The same description applies to the bottom plots, for the summer-like simulations without the ice signature. In both cases the LRM_LIT retracker gives unbiased LIT results. The uncertainty of the LIT retrieval from the winter-like simulations is ~10 cm.

LIT retrievals from satellite missions have been evaluated against LIT simulations from the thermodynamic lake ice model CLIMo (Duguay et al., 2003). A qualitative comparison with in-situ data was also performed when possible[1]. Figure 21 provides an example of the comparison of the LIT estimations obtained within a winter season over Great Slave Lake with the LRM_LIT retracker applied to Jason-2 data (blue triangles) and Jason-3 data (red stars) and LIT from CLIMo simulations with different on-ice snow depth scenarios (diamonds) and in-situ data (circles). There is an excellent agreement between Jason-2 and Jason-3 LIT estimates, which are fully compatible with the thermodynamic simulations and qualitatively in agreement with in-situ data. We note that, in general, the LIT melting phase is detected earlier with the satellite-based measurements because of snow melting that perturbs the radar echoes.

[1] It is worth noting that the comparison between LIT estimates from satellite missions and in-situ data must be taken with caution. In-situ data are typically collected near the shore, while satellite data are taken from the middle of the lake to avoid land contamination. These can represent different environments in terms of bathymetry, wind exposure, snow type and quantity. All these parameters play a key role on ice formation and thickness and they can lead to significant LIT differences.

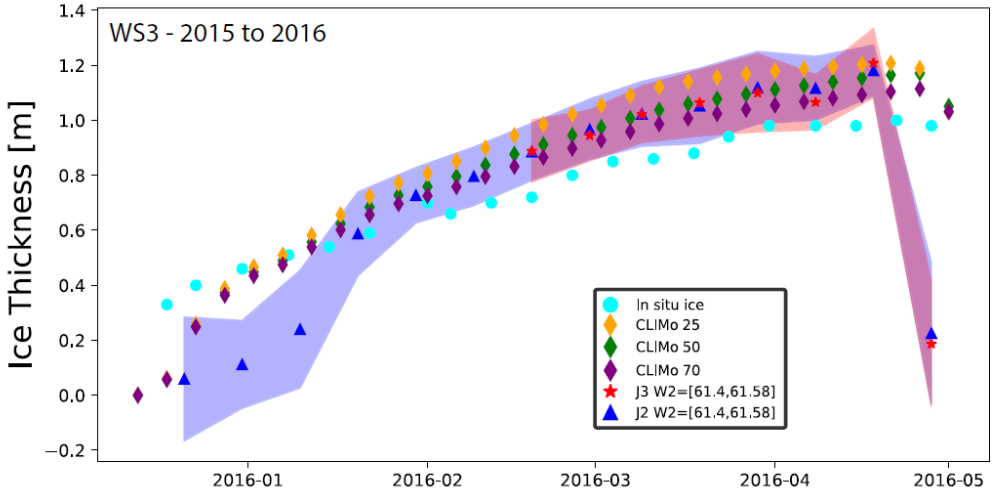

Figure 21 LIT estimates over Great Slave Lake for the 2015-16 winter season. Shown are a comparison between LIT estimates with the LRM_LIT retracker from Jason-2 (triangles) and Jason-3 (stars) data, CLIMo simulations (diamonds) and in-situ data (circles). The shaded areas correspond to the LIT estimation uncertainties computed from Jason-2 data (blue) and Jason-3 data (red). Three different realizations of CLIMo simulations are shown by varying the amount of snow on the ice. The in-situ data consist of ice thickness measurements collected in Back Bay near Yellowknife

To quantify the comparison between the LIT estimates from Jason-2, Jason-3 and CLIMo, two statistics are computed, the MBE:

$$MBE = \frac{1}{N}\sum_{i}^{N}(LIT_i^{J2} - LIT_i^{DS}) \qquad [7.1]$$

And the RMSE:

$$RMSE = \sqrt{\frac{1}{N}\sum_{i}^{N}(LIT_i^{J2} - LIT_i^{DS})^2} \qquad [7.2]$$

of the LIT estimates derived from Jason-2, LIT^{J2}_i , and the other data sets, LIT^{DS}_i , for the N measurements obtained in the middle of the winter season. In the illustrative case of the 2015-16 winter season shown in Figure 21, agreement between the Jason-2 (blue triangles) and Jason-3 (red stars) LIT measurements is excellent. In the middle of the ice season, the MBE is only 0.013 m and the RMSE is 0.024 m between the two data sets. Also, the difference in the LIT mean value is only 0.02 m and that of maximum LIT is 0.025 m. Both Jason-2 and Jason-3 LIT are in strong agreement with the thermodynamics simulations with 50% of snow on ice as input (CLIMo-50 simulations), in particular in the middle of the ice season where the MBE between Jason-2 and CLIMo-50 is less than 0.01 m and the RMSE is 0.019 m. Overall, these results demonstrate that LIT estimates can be retrieved from radar altimetry data that are compatible with thermodynamic simulations and qualitatively in agreement with in-situ measurements.

Finally, the superposition of the LIT retrievals on RADARSAT-2 synthetic aperture radar (SAR) and MODIS optical images allows for a better assessment of the consistency of the LIT estimates as they provide valuable information about the state of the ice and overlaying snow cover. Figure 22 shows (left column from top to bottom) the Jason-2 LIT estimates superimposed on RADARSAT-2/MODIS images obtained within one day of Jason-2 overpasses in December, February, March and end of April. The ice thickness is colour coded and ranges from no or thin ice (0-0.32 m) in light blue to LIT in the range of 1.28- 1.60 m in pink. Plots on the right-hand side of Figure 22, show the spatial evolution of the Jason-2 LIT estimates (top plots) and the corresponding evolution of the reduced chi-squared statistics as a function of the latitude (bottom plots) for the same dates as in the left column.

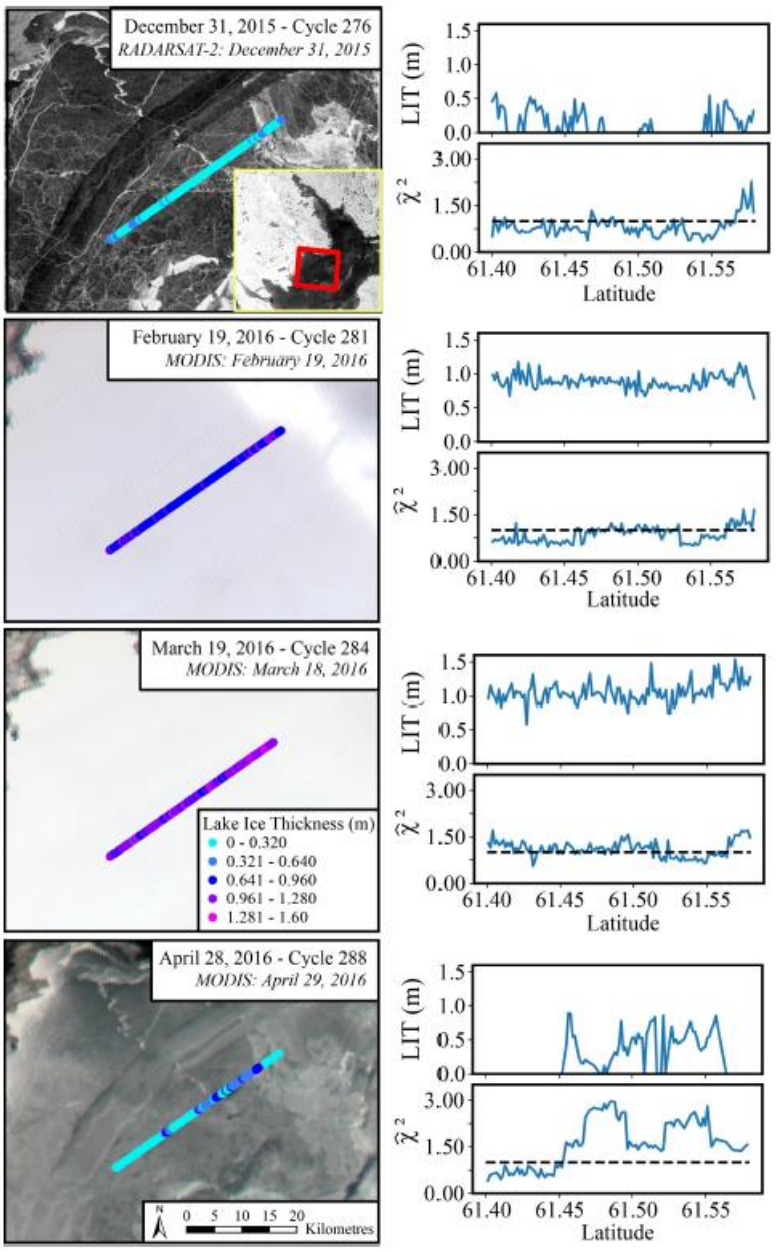

Figure 22: Evolution of Jason-2 LIT estimates over Great Slave Lake along track 45 for WS3 (winter season 2015-2016). Plots in the left column show, from top to bottom, along-track Jason-2 LIT estimates superimposed on MODIS images on the same date or within one day in December, February, March and end of April. Plots in the right column show the evolution of the Jason-2 LIT estimates as a function of latitude (top plots) and of the reduced chi-squared statistics as a function of the latitude (bottom plots) along the track

7.3 Identified issues

- The LRM_LIT retracker can capture the seasonal transitions of ice forming and melting but cannot precisely follow the ice evolution at the transitions because of the difficulty of retracking heterogeneous surfaces when the ice is too thin and when snow on the ice surface begins to melt.
- The LRM_LIT retracker works if the ice related signature, that is, the step like feature in the leading edge of the radar waveforms, is present. This signature in the LRM waveform data depends on the properties and thickness of the snowpack and the ice layer and could be erased if some conditions are not met, as for instance in the case of snow-free lake ice or melting snow

on the ice surface. Therefore, there could be lakes for which the ice signature is not clearly marked or not present. In this case, these targets could not be analysed with the LRM_LIT retracker.

7.4 References

Beckers, J. F., J. Alec Casey, and C. Haas. (2017). Retrievals of lake ice thickness from Great Slave Lake and Great Bear Lake using CryoSat-2. *IEEE Transactions on Geoscience and Remote Sensing* 55(7): 3708–3720.

Kang, K.-K., C. R. Duguay, S. E. L. Howell, C. Derksen, and R. Kelly. (2010). Sensitivity of AMSR-E brightness temperatures to the seasonal evolution of lake ice thickness. *IEEE Geoscience and Remote Sensing Letters* 7(4): 751–755.

Kang, K.-K., C. Duguay, J. Lemmetyinen, and Y. Gel. (2014). Estimation of ice thickness on large northern lakes from AMSR-E brightness temperature measurements. *Remote Sensing of Environment* 150: 1–19.

Kheyrollah Pour, H., C. R. Duguay, K. A. Scott, and K.- K. Kang. (2017). Improvement of Lake Ice Thickness Retrieval From MODIS Satellite Data Using a Thermodynamic Model. *IEEE Transactions on Geoscience and Remote Sensing* 55(10): 5956–5965.

Mangilli, A., P. Thibaut, C. R. Duguay and J. Murfitt. (2022). A New Approach for the Estimation of Lake Ice Thickness From Conventional Radar Altimetry. *IEEE Transactions on Geoscience and Remote Sensing* 60: 1-15, 4305515. https://doi.org/10.1109/TGRS.2022.3197109

Shu, S., H. Liu, R. A. Beck, F. Frappart, J. Korhonen, M. Xu, B. Yang, K. M. Hinkel, Y. Huang, and B. Yu. (2020). Analysis of Sentinel-3 SAR altimetry waveform retracking algorithms for deriving temporally consistent water levels over ice-covered lakes. *Remote Sensing of Environment* 239: 111643.

Yang, Y., P. Moore, Z. Li, and F. Li. (2021). Lake level change from satellite altimetry over seasonally ice-covered lakes in the Mackenzie River Basin. *IEEE Transactions on Geoscience and Remote Sensing* 59 (10): 8143–8152.

8 Inter-product consistency

8.1 Inter-product consistency checks for CRDP v2.1

Consistency checks previously covered combinations of LWLR, LSWT and LIC. Results were reported in the previous issue of this document and integrated into baseline processing for LWLR in v2.1. Further consistency checks now focus on LIT as it enters the baseline processing phase. Consistency checks tend to analyse the latest-available version of the products for comparison, so may refer back to v2.0.2.

LIT products can be checked against LSWT and LIC products for inter-variable consistency. The consistency of all three products will govern the expected and observed relationships between these variables. The following algorithms are developed on the spatial subsets which are defined by the footprints of the LIT calculation. The analysis is therefore restricted to three areas of Great Slave Lake.

8.1.1 Consistency of LIT versus LSWT

All LSWT data points of the Lake-CCI product (v2.0.2) within the footprint area are extracted, if they exceed a quality value of 3. Daily weighted mean values of LSWT are calculated with respect to their uncertainties.

The weights w are defined as $w = 1/lswt_{unc}^2$
and the weighted daily mean ***wlswt*** as $wlswt = \frac{1}{\sum w}\sum w \cdot lswt.$

The uncertainty of wlswt (***wlswt_unc***) is defined as the square root of the weighted variance:

$$wlswt_{unc} = \sqrt{\frac{1}{\sum w}\sum w_i * (lswt_i - wlswt)^2}$$

The following consistency categories have been defined for a daily value of lake ice thickness ***lit*** and its uncertainty ***lit_unc*** (with lit>0 and lit_unc>0):

- All cases, which can be considered *consistent*:
  - *wlswt* is not available AND lit-lit_unc>0. The lower bound of lake ice thickness is positive and no lake surface water temperature has been observed.
  - wlswt is not available AND (lit-lit_unc < 0 <lit+lit_unc). Lake ice thickness is always positive; therefore, most of the lit interval suggests a positive lake ice thickness, while no lake surface water temperature has been observed.
  - $wlswt - wlswt_{unc} < 273.15$ AND lit-lit_unc > 0. Lake water temperature has been observed, but the lower boundary is below the freezing point and lower boundary of lake ice thickness is positive.
- Minor cases of inconsistency:
  - $wlswt - wlswt_{unc} < 273.15$ AND (lit-lit_unc < 0 <lit+lit_unc).
  - $wlswt - wlswt_{unc} > 273.15$ AND lit-lit_unc <0. The lower bound of the lake water temperature is above freezing point and lake ice thickness exists.
- Inconsistent:
  - $wlswt - wlswt_{unc} > 273.15$ AND lit-lit_unc > 0. The lower bound of lake water temperature is above freezing point and the lower bound of lake ice thickness is positive. There is a physical contradiction in such cases.

8.1.2 Consistency of LIT versus LIC

All LIC data points of the Lake-CCI product (v2.0.2) within the footprint area are extracted. The daily counts of the classification classes water, ice, cloud and bad are noted.

The consistency categories for lake ice thickness (lit>0) against the LIC are defined as:

- Consistent: $N_{ice} > 0$ & $N_{water} == 0$. The daily count of LIC finds only ice, no water.
- Minor cases of inconsistency (with $N_{ice} > 0$, $N_{water} > 0$):
  - $N_{ice} > N_{water}$. LIC identifies more ice pixels than water pixels.
  - $N_{water} > N_{ice}$. LIC identifies more water pixels than ice pixels.
- Inconsistent: $N_{water} > 0$ & $N_{ice} == 0$. Although a lake ice thickness is observed, the LIC finds only water, no ice.

8.2 Validation results

In general, the consistency of the LIT product compared to LSWT and LIC is very good and follows scientific expectations.

8.2.1 LIT versus LSWT

For most periods, the time series of LIT and LSWT do not overlap. As expected, the products are mutually exclusive, except for very few coinciding measurements during ice formation or break down.

For Pass 45 only two dates are found which are inconsistent according to the defined criteria (Figure 23). In the first case (2010-05-28, Figure 24 upper panel) very little coverage is available for the LSWT product, which results in little representativity of the mean value 273.646 +/- 0.051K. Values fall within a very small range, which leads to a small uncertainty for wlswt. A case like this should most likely be considered consistent.

The second case (2016-12-02, Figure 24 lower panel) is more likely to show a real inconsistency. The mean LSWT is 275.88 +/-0.36 K and LIT is 0.47+/-0.08 m. Even the classification suggests water instead of ice.

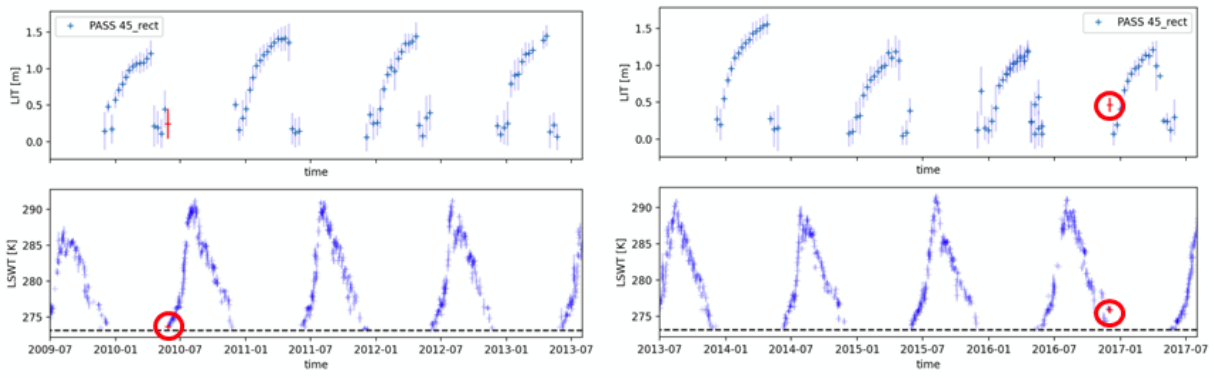

Figure 23: Time series of lake ice thickness (with uncertainty) and daily weighted mean LSWT (with uncertainty) of Pass 45. Two dates are found which are inconsistent.

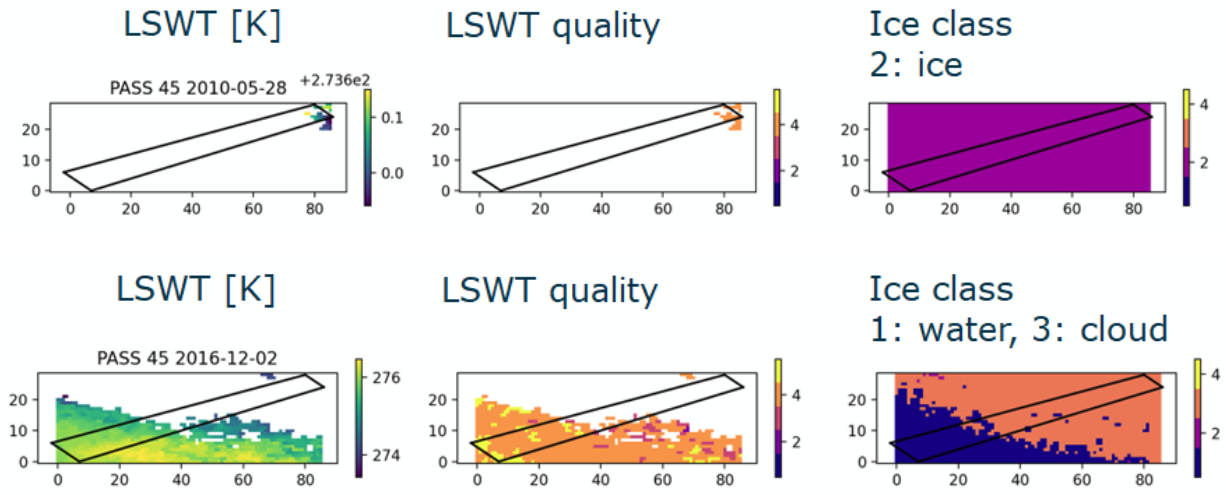

Figure 24: LSWT and LIC data for the dates with inconsistency. Mean values and counts are taken from the marked area of interest.

For the other two passes (178 and 254) the consistency is color-coded within the timeseries of LIT (Figure 25). In pass 178 minor inconsistencies are discovered 7 times, and 4 times an inconsistency is discovered. (There are some days with two LIT values.) Pass 254 includes 4 cases of minor inconsistency and 2 cases of inconsistency.

Most of these cases occur during ice break up.

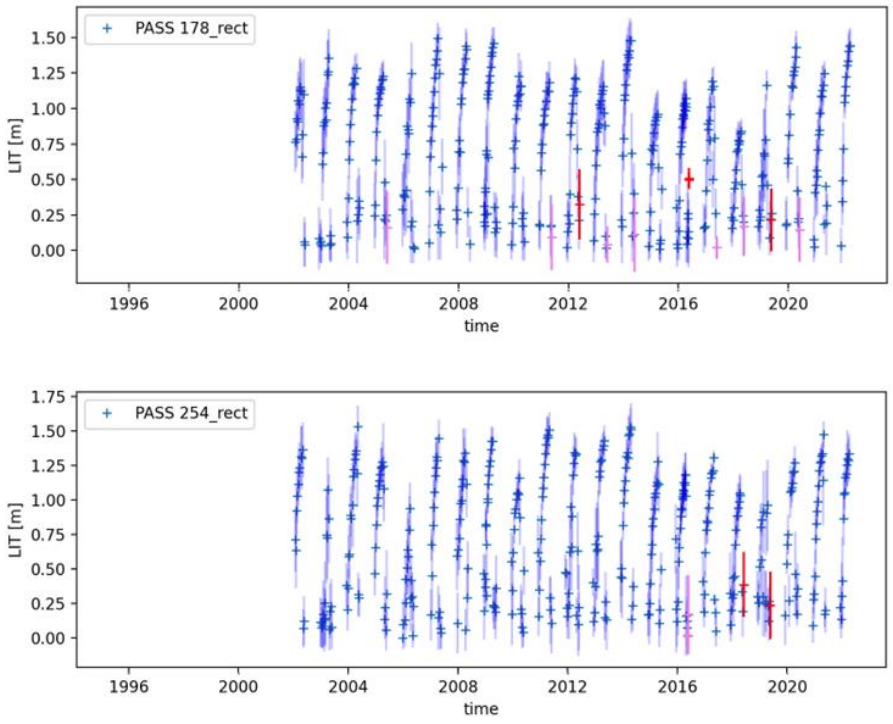

Figure 25 Timeseries of LIT for passes 178 and 254. Consistency is coded by color: consistent (blue), minor inconsistency (violet), inconsistent (red).

8.2.2 LIT versus LIC

In most cases when LIT and LIC are available at the same time, the classification finds ice in the area of interest (blue dots in lower panel of Figure 26). For each pass the number of cases with minor inconsistency is largest, in which ice and water pixels are present, and more ice than water pixels have been counted (see Table 19). They can occur throughout the entire ice period, slightly more often during ice formation than during break up, which can be expected. There are fewer cases when the number of pixels in the water class exceeds the ice counts.

The cases, when the classification identifies only water pixel coinciding with LIT, are probably pointing towards an inconsistency in the identification of ice in the LIC product.

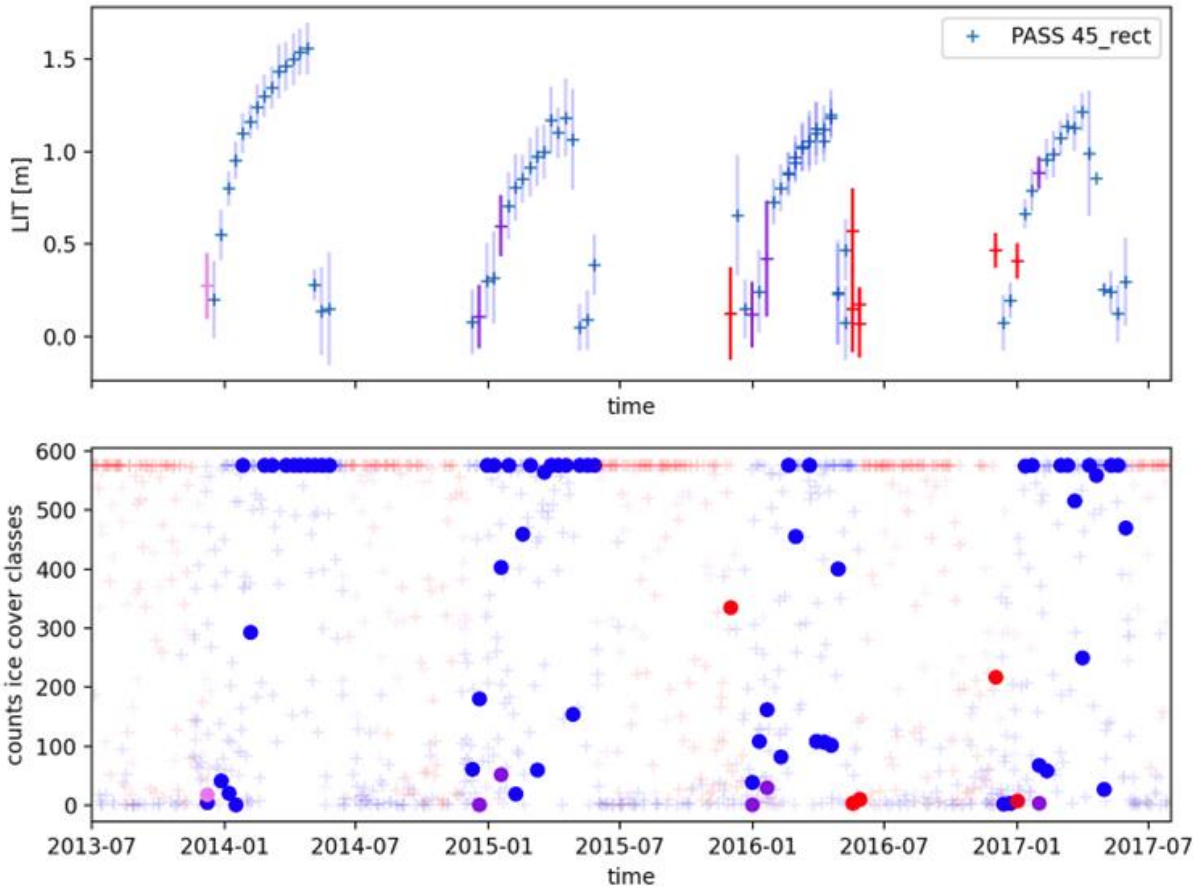

Figure 26: Timeseries of LIT and LIC counts for pass 54 (example). Consistency is coded by colour: consistent (blue), minor inconsistency N_ice>N_water (bluepurple), minor inconsistency N_water>N_ice (violet), inconsistent (red). Bottom panel: dots mark dates, when LIT and LIC are available.

Table 19 Summary of occurrence of different kinds of inconsistencies between LIT and LIC.

Pass No	N_ice > N_water	N_water>N_ice	Only N_water
45	20	4	10
178	30	5	6
254	20	4	1

8.3 Identified issues

For LIT versus LSWT it can be discussed which cases should be considered consistent.

The relative number of valid pixels inside the area of interest with respect to full coverage could be considered as a value of representativity both for LIC and LSWT. Small coverage means low representativity and therefore consistency (or inconsistency) becomes more uncertain.

The LIT versus LIC definitions do not include the uncertainty in LIT yet.

Appendix A - List of acronyms

AATSR	Advanced Along Track Scanning Radiometer
AATSR	Advanced Along Track Scanning Radiometer
AERONET-OC	Aerosol Robotic NETwork – Ocean Color
AMI	Active Microwave Instrument
AMSR-E	Advanced Microwave Scanning Radiometer for EOS
APP	Alternating Polarization mode Precision
ASAR	Advanced Synthetic Aperture Radar
ASLO	Association for the Sciences of Limnology and Oceanography
ATBD	Algorithm Theoretical Basis Document
ATSR	Along Track Scanning Radiometer
AVHRR	Advanced very-high-resolution radiometer
BAMS	Bulletin of the American Meteorological Society
BC	Brockman Consult
C3S	Copernicus Climate Change Service
CCI	Climate Change Initiative
CDR	Climate Data Record
CDOM	Coloured Dissolved Organic Matter
CEDA	Centre for Environmental Data Archival
CEMS	Centre for Environmental Monitoring from Space
CEOS	Committee on Earth Observation Satellites
CGLOPS	Copernicus Global Land Operation Service
CIS	Canadian Ice Service
CLS	Collecte Localisation Satellite
CMEMS	Copernicus Marine Environment Monitoring Service
CMUG	Climate Modelling User Group
CNES	Centre national d'études spatiales
CNR	National Research Council of Italy
CORALS	Climate Oriented Record of Altimetry and Sea-Level
CPD	Communication Plan Document
CR	Cardinal Requirement
CRG	Climate Research Group
CSWG	Climate Science Working Group
CTOH	Center for Topographic studies of the Ocean and Hydrosphere
DOC	Dissolved Organic Carbon
DUE	Data User Element
ECMWF	European Centre for Medium-Range Weather Forecasts
ECV	Essential Climate Variable
ELLS-IAGRL	European Large Lakes Symposium-International Association for Great Lakes Research
ENVISAT	Environmental Satellite
EO	Earth Observation
EOMORES	Earth Observation-based Services for Monitoring and Reporting of Ecological Status
ERS	European Remote-Sensing Satellite
ESA	European Space Agency
ESRIN	European Space Research Institute
ETM+	Enhanced Thematic Mapper Plus
EU	European Union
EUMETSAT	European Organisation for the Exploitation of Meteorological Satellites
FAQ	Frequently Asked Questions
FCDR	Fundamental Climate Data Record

FIDUCEO	Fidelity and Uncertainty in Climate data records from Earth Observations
FP7	Seventh Framework Programme
GAC	Global Area Coverage
GCOS	Global Climate Observing System
GEMS/Water	Global Environment Monitoring System for freshwater
GEO	Group on Earth Observations
GEWEX	Global Energy and Water Exchanges
GloboLakes	Global Observatory of Lake Responses to Environmental Change
GLOPS	Copernicus Global Land Service
GTN-H	Global Terrestrial Network – Hydrology
GTN-L	Global Terrestrial Network – Lakes
H2020	Horizon 2020
HYDROLARE	International Data Centre on Hydrology of Lakes and Reservoirs
ILEC	International Lake Environment Committee
INFORM	Index for Risk Management
IPCC	Intergovernmental Panel on Climate Change
ISC	International Science Council
ISO	International Organization for Standardization
ISRO	Indian Space Research Organisation
JRC	Joint Research Centre
KPI	Key Performance Indicators
LEGOS	Laboratoire d'Etudes en Géophysique et Océanographie Spatiales
LIC	Lake Ice Cover
LIT	Lake Ice Thickness
LSC	Lake Storage Change
LSWT	Lake Surface Water Temperature
LWE	Lake Water Extent
LWL	Lake Water Level
LWLR	Lake Water Leaving Reflectance
MERIS	MEdium Resolution Imaging Spectrometer
MGDR	Merged Geophysical Data Record
MODIS	Moderate Resolution Imaging Spectroradiometer
MSI	MultiSpectral Instrument
MSS	MultiSpectral Scanner
NASA	National Aeronautics and Space Administration
NERC	Natural Environment Research Council
NetCDF	Network Common Data Form
NOAA	National Oceanic and Atmospheric Administration
NSERC	Natural Sciences and Engineering Research Council
NSIDC	National Snow & Ice Data Center
NTU	Nephelometric Turbidity Unit
NWP	Numerical Weather Prediction
OLCI	Ocean and Land Colour Instrument
OLI	Operational Land Imager
OSTST	Ocean Surface Topography Science Team
PML	Plymouth Marine Laboratory
PP	Payment Plan
PRISMA	PRecursore IperSpettrale della Missione Applicativa
Proba	Project for On-Board Autonomy
QSR	Quarterly Status Report
R	Linear Correlation Coefficient
RA	Radar Altimeter
RMSE	Root Mean Square Error

SAF	Satellite Application Facility
SAR	Synthetic Aperture Radar
SeaWIFS	Sea-viewing Wide Field-of-view Sensor
SIL	International Society of Limnology
SLSTR	Sea and Land Surface Temperature Radiometer
SoW	Statement of Work
SPONGE	SPaceborne Observations to Nourish the GEMS
SRD	System Requirements Document
SSD	System Specification Document
SST	Sea Surface Temperature
STSE	Support To Science Element
SWOT	Surface Water and Ocean Topography
TAPAS	Tools for Assessment and Planning of Aquaculture Sustainability
TB	Brightness Temperature
TM	Thematic Mapper
TOA	Top Of Atmosphere
TR	Technical Requirement
UNEP	United Nations Environment Programme
UoR	University of Reading
UoS	University of Stirling
US	United States
VIIRS	Visible Infrared Imaging Radiometer Suite
WCRP	World Climate Research Program
WHYCOS	World Hydrological Cycle Observing Systems
WMO	World Meteorological Organization
WP	Work Package